



CHICAGO JOURNALS



GASPS—A Herschel Survey of Gas and Dust in Protoplanetary Disks: Summary and Initial Statistics

Author(s): W. R. F. Dent, W. F. Thi, I. Kamp, J. P. Williams, F. Menard, S. Andrews, D. Ardila, G. Aresu, J.-C. Augereau, D. Barrado y Navascues, S. Brittain, A. Carmona, D. Ciardi, W. Danchi, J. Donaldson, G. Duchene, C. Eiroa, D. Fedele, C. Grady, I. de Gregorio-Molsalvo, C. Howard, N. Huélamo, A. Krivov, J. Lebreton, R. Liseau, C. Martin-Zaidi, G. Mathews, G. Meeus, I. Mendigutía, B. Montesinos, M. Morales-Calderon, A. Mora, H. N ...

Source: *Publications of the Astronomical Society of the Pacific*, Vol. 125, No. 927 (May 2013), pp. 477-505

Published by: [The University of Chicago Press](#) on behalf of the [Astronomical Society of the Pacific](#)

Stable URL: <http://www.jstor.org/stable/10.1086/670826>

Accessed: 09/07/2013 16:21

Your use of the JSTOR archive indicates your acceptance of the Terms & Conditions of Use, available at <http://www.jstor.org/page/info/about/policies/terms.jsp>

JSTOR is a not-for-profit service that helps scholars, researchers, and students discover, use, and build upon a wide range of content in a trusted digital archive. We use information technology and tools to increase productivity and facilitate new forms of scholarship. For more information about JSTOR, please contact support@jstor.org.



The University of Chicago Press and Astronomical Society of the Pacific are collaborating with JSTOR to digitize, preserve and extend access to *Publications of the Astronomical Society of the Pacific*.

<http://www.jstor.org>

GASPS—A Herschel Survey of Gas and Dust in Protoplanetary Disks: Summary and Initial Statistics

W. R. F. DENT,¹ W. F. THI,^{2,3} I. KAMP,² J. P. WILLIAMS,⁴ F. MENARD,³ S. ANDREWS,⁵ D. ARDILA,⁶ G. ARESU,²
J.-C. AUGEREAU,³ D. BARRADO Y NAVASCUES,^{7,8} S. BRITAIN,⁹ A. CARMONA,³ D. CIARDI,¹⁰ W. DANCHI,¹¹
J. DONALDSON,¹² G. DUCHENE,^{3,13} C. EIROA,¹⁴ D. FEDELE,¹⁵ C. GRADY,¹⁶ I. DE GREGORIO-MOLSALVO,¹
C. HOWARD,¹⁷ N. HUÉLAMO,⁷ A. KRIVOV,¹⁸ J. LEBRETON,³ R. LISEAU,¹⁹ C. MARTIN-ZAIDI,³ G. MATHEWS,⁴
G. MEEUS,¹⁴ I. MENDIGUTÍA,⁷ B. MONTESINOS,⁷ M. MORALES-CALDERON,⁷ A. MORA,²⁰ H. NOMURA,²¹
E. PANTIN,²² I. PASCUCCI,²³ N. PHILLIPS,¹ C. PINTE,³ L. PODIO,¹ S. K. RAMSAY,²⁴ B. RIAZ,²⁵
P. RIVIERE-MARICHALAR,⁷ A. RÖBERGE,¹¹ G. SANDELL,¹⁷ E. SOLANO,⁷
I. TILLING,²⁶ J. M. TORRELLES,²⁷ B. VANDENBUSCHE,²⁸ S. VICENTE,²
G. J. WHITE,^{29,30} AND P. WOITKE³¹

Received 2012 December 31; accepted 2013 April 01; published 2013 May 31

ABSTRACT. We describe a large-scale far-infrared line and continuum survey of protoplanetary disk through to young debris disk systems carried out using the ACS instrument on the Herschel Space Observatory. This Open Time Key program, known as GASPS (Gas Survey of Protoplanetary Systems), targeted ~250 young stars in narrow wavelength regions covering the [OI] fine structure line at 63 μm the brightest far-infrared line in such objects. A subset of the brightest targets were also surveyed in [OI]145 μm , [CII] at 157 μm , as well as several transitions of H₂O and high-excitation CO lines at selected wavelengths between 78 and 180 μm . Additionally, GASPS included continuum photometry at 70, 100 and 160 μm , around the peak of the dust emission. The targets were SED Class II–III T Tauri stars and debris disks from seven nearby young associations, along with a comparable sample of isolated

¹ ALMA SCO, Alonso de Cordova 3107, Vitacura, Santiago, Chile.

² Kapteyn Astronomical Institute, Postbus 800, 9700 AV Groningen, The Netherlands.

³ UJF-Grenoble 1/CNRS-INSU, Institut de Plantologie et d’Astrophysique de Grenoble (IPAG) UMR 5274, Grenoble F-38041, France.

⁴ Institute for Astronomy, University of Hawaii at Manoa, Honolulu, HI.

⁵ Harvard-Smithsonian Center for Astrophysics, 60 Garden Street, Cambridge, MA.

⁶ NASA Herschel Science Center, Caltech, 1200 E. California Blvd., Pasadena, CA.

⁷ Centro de Astrobiología-Depto. Astrofísica (CSIC-INTA), ESAC Campus, PO Box 78, E-28691 Villanueva de la Cañada, Spain.

⁸ Calar Alto Observatory, Centro Astronómico Hispano Alemán, C/Jesús Durbán Remón, E-04004 Almera, Spain.

⁹ Department of Physics and Astronomy, 118 Kinar Laboratory, Clemson University, Clemson, SC.

¹⁰ NASA Exoplanet Science Institute, Caltech, Pasadena, CA.

¹¹ NASA Goddard Space Flight Center, Exoplanets and Stellar Astrophysics Laboratory, Code 667, Greenbelt, MD.

¹² Department of Astronomy, University of Maryland, College Park, MD.

¹³ Astronomy Department, University of California, Berkeley, CA.

¹⁴ Dep. de Física Teórica, Fac. de Ciencias, UAM Campus Cantoblanco, Madrid, Spain.

¹⁵ Max Planck Institut für Extraterrestrische Physik, Giessenbachstrasse 1, Garching, Germany.

¹⁶ Eureka Scientific, 2452 Delmer, Suite 100, Oakland, CA.

¹⁷ SOFIA-USRA, NASA Ames Research Center, MS 232-12, Building N232, Rm. 146, PO Box 1, Moffett Field, CA.

¹⁸ Astrophysikalisches Institut, Friedrich-Schiller-Universität Jena, Schillergässchen 2-3, Jena, Germany.

¹⁹ Department of Earth and Space Sciences, Chalmers University of Technology, Onsala Space Observatory, Onsala, Sweden.

²⁰ ESA-ESAC Gaia SOC, PO Box 78, 28691 Villanueva de la Cañada, Madrid, Spain.

²¹ Department of Astronomy, Graduate School of Science, Kyoto University, Kyoto 606-8502, Japan.

²² Laboratoire AIM, CEA/DSM-CNRS-Université Paris Diderot, IRFU/Sap, CE Saclay, France.

²³ Lunar and Planetary Laboratory, University of Arizona, Tucson, AZ.

²⁴ European Southern Observatory, Karl-Schwarzschild-Strasse 2, 85748 Garching bei München, Germany.

²⁵ Centre for Astrophysics Research, University of Hertfordshire, Hatfield, UK.

²⁶ University of Edinburgh, Royal Observatory, Edinburgh, Blackford Hill, Edinburgh, UK.

²⁷ CSIC-UB/IEEC, Universitat de Barcelona, Martí Franquès 1, Barcelona, Spain.

²⁸ Instituut voor Sterrenkunde, Katholieke Universiteit Leuven, Celestijnenlaan 200D, Heverlee, Belgium.

²⁹ Department of Physical Sciences, Open University, Milton Keynes, UK.

³⁰ RALSpace, Rutherford Appleton Laboratory, Chilton, Didcot OX11 0NL, UK.

³¹ SUPA, School of Physics and Astronomy, University of St. Andrews, North Haugh, St. Andrews, KY16 9SS, UK.

Herbig AeBe stars. The aim was to study the global gas and dust content in a wide sample of circumstellar disks, combining the results with models in a systematic way. In this overview paper we review the scientific aims, target selection and observing strategy of the program. We summarise some of the initial results, showing line identifications, listing the detections, and giving a first statistical study of line detectability. The [OI] line at $63\ \mu\text{m}$ was the brightest line seen in almost all objects, by a factor of ~ 10 . Overall [OI] $63\ \mu\text{m}$ detection rates were 49%, with 100% of HAeBe stars and 43% of T Tauri stars detected. A comparison with published disk dust masses (derived mainly from sub-mm continuum, assuming standard values of the mm mass opacity) shows a *dust* mass threshold for [OI] $63\ \mu\text{m}$ detection of $\sim 10^{-5}\ M_{\odot}$. Normalising to a distance of 140 pc, 84% of objects with dust masses $\geq 10^{-5}\ M_{\odot}$ can be detected in this line in the present survey; 32% of those of mass 10^{-6} – $10^{-5}\ M_{\odot}$, and only a very small number of unusual objects with lower masses can be detected. This is consistent with models with a moderate UV excess and disk flaring. For a given disk mass, [OI] detectability is lower for M stars compared with earlier spectral types. Both the continuum and line emission was, in most systems, spatially and spectrally unresolved and centred on the star, suggesting that emission in most cases was from the disk. Approximately 10 objects showed resolved emission, most likely from outflows. In the GASPS sample, [OI] detection rates in T Tauri associations in the 0.3–4 Myr age range were $\sim 50\%$. For each association in the 5–20 Myr age range, ~ 2 stars remain detectable in [OI] $63\ \mu\text{m}$, and no systems were detected in associations with age > 20 Myr. Comparing with the total number of young stars in each association, and assuming a ISM-like gas/dust ratio, this indicates that $\sim 18\%$ of stars retain a gas-rich disk of total mass $\sim 1\ M_{\text{Jupiter}}$ for 1–4 Myr, 1–7% keep such disks for 5–10 Myr, but none are detected beyond 10–20 Myr. The brightest [OI] objects from GASPS were also observed in [OI] $145\ \mu\text{m}$, [CII] $157\ \mu\text{m}$ and CO $J = 18 - 17$, with detection rates of 20–40%. Detection of the [CII] line was not correlated with disk mass, suggesting it arises more commonly from a compact remnant envelope.

1. INTRODUCTION

One of the most significant astronomical discoveries of the past decade has been the realisation that roughly 20% of main-sequence FGK stars harbor planets (Fischer & Valenti 2005; Borucki et al. 2011). Moreover, at least 16% of FGK main-sequence stars are found to have a debris disk more massive than the dust in our own Solar System, indicating an unseen population of colliding planetesimals (Trilling et al. 2008; Wyatt 2008). These two independent results imply that the planet and planetesimal formation process is common and robust, and can lead to a wide diversity of systems. However, it is not clear how young gas-rich disks—where planet formation is either still occurring or has recently completed—evolve into mature planetary and/or debris disk systems.

Both debris disks and main sequence planetary systems are gas-poor. Debris systems, composed of grains in a collisional cascade, have dust masses of $\leq 10^{-7}\ M_{\odot}$, although the mass of planetesimals—thought to be the starting point of the cascade—may be $10^{-4}\ M_{\odot}$ or more (Wyatt & Dent 2002). In most cases, no molecular gas is detected (Dent et al. 1995); however, in a very few nearby young debris systems such as β Pic, a small mass of mostly atomic gas is seen (Lagrange et al. 1998; Olofsson et al. 2001; Roberge et al. 2006). Possible gas formation mechanisms in such systems are secondary release during grain–grain collisions (Thébaud & Augereau 2005), photodesorption from dust grains (Chen et al. 2007), or sublimation from comets (Zuckerman & Song 2012).

By contrast, the material around young, pre-main-sequence (but optically-visible) stars is gas-rich. Such so-called proto-planetary disks are found towards $\sim 10\%$ of stars aged 5 Myr,

and at least 80% of stars aged < 1 Myr (Haisch et al. 2001). Similar in size to debris disks, their *dust* masses are typically 10^{-5} – $10^{-3}\ M_{\odot}$. The assumption normally made is that 99% of the disk mass is gas, the same as that of the natant interstellar cloud, leading to these disks being described as ‘primordial’. Their total masses would then be similar to that of the minimum mass Solar Nebula (Williams & Cieza 2011). In the even younger, so-called ‘protostellar’ stage (typically ≤ 0.1 Myr), disk masses may be still larger, approaching that of the protostar itself. Systems at this phase are usually optically obscured, as the remnant cloud and infalling envelope have not yet dispersed.

Dissipation of the primordial disk gas limits the timescale for giant planet formation, affects the dynamics of planetary bodies of all sizes during their formation, and determines the final architecture and constitution of planetary systems. No planet formation will take place without gas to damp the particle velocities. The methods for removal of the gas and dust components are generally different. Photoevaporation is thought to be important in gas dissipation (Gorti & Hollenbach 2004, 2009), and bipolar outflow jets may also play a role. Molecular species will also be depleted in regions exposed to the photodestructive effects of UV (Kamp & Sammar 2004). Selective removal of the dust can be caused by the interaction with a planet (Rice et al. 2006), ice or refractory grain sublimation (Thi et al. 2005), or by grain growth and settling (Dullemond & Dominik 2005). As noted by these authors, these effects can be very rapid, occurring on timescales $\sim 10^4$ yr—significantly shorter than the disk ages.

Statistical studies show that the presence of Jupiter-mass planets in mature systems is strongly influenced by stellar metallicity, mass, and binary companions (Fischer & Valenti 2005;

Johnson et al. 2007). Do the stellar parameters also affect disks? Age clearly affects the fraction of stars with primordial disks (Haisch et al. 2001) and, on a longer timescale, debris disks (Carpenter et al. 2009). Disks may be affected by binary companions in debris systems (Trilling et al. 2007) but not substantially by stellar metallicity in debris or protoplanetary systems (Greaves et al. 2006; D’Orazi et al. 2011; Maldonado et al. 2012). And although there appears to be no direct correlation between debris disks and planets (Bryden et al. 2009), there are clearly some systems which have both, and where the planet creates a gap or affects the disk shape (Kalas et al. 2008; Thalmann et al. 2010; Hughes et al. 2011). At present, there is no clear observational evidence that primordial disk lifetimes are significantly affected by the stellar mass (Boissier et al. 2011; Ercolano et al. 2011).

To study disk evolution and look for general trends, many large and unbiased dust continuum surveys have been carried out, e.g., in the near-infrared (Kenyon & Hartmann 1995; Haisch et al. 2001), the mid- to far-infrared (most complete out to a wavelength of 70 μm in the Spitzer projects FEPS [Hillenbrand et al. 2008] and c2d [Evans et al. 2009]), and in the sub-mm (Andrews & Williams 2005). They indicate primordial disk lifetimes of a few Myr, but there is a broad distribution of dust mass at any particular age, with notable outliers. For example, although the fraction of disk-bearing stars in the ~ 1 Myr-old Taurus star-forming region is as high as 75%, a significant minority of its stars have no detectable dust excess (Luhman et al. 2010).

Dust emission is ostensibly easy to interpret, as the normally optically-thin sub-mm continuum can be used to directly estimate the dust mass, M_d , by employing a mass opacity, κ_ν , and emissivity power law, β . Typical values adopted in the literature are $\kappa_\nu = 1.7 \text{ g cm}^{-2}$ and $\beta = 1.0$ (Andrews & Williams 2005). However, κ_ν depends on the grain size distribution (D’Alessio et al. 2006), and most of the solid body mass may be in large grains contributing little to the observed flux (Wyatt & Dent 2002; Krivov et al. 2008). One option is to define a dust mass which only includes solid material smaller than 1 mm (Thi et al. 2010); this is reasonably consistent with the standard literature value of κ_ν . Deriving the *total* disk mass requires an assumption of the gas-to-dust ratio; normally the interstellar medium value of 100 is used, but it is unclear whether this value is maintained in disks (and it is certainly not valid for debris-dominated systems). Throughout most of this current work, we have quoted disk masses in terms of the *dust* mass, M_d , allowing comparisons to be made independently of the gas/dust ratio.

Although gas dominates the mass (at least for protoplanetary disks), emission lines are generally more difficult than the continuum to both observe and interpret. The bulk of the gas is in H_2 which has no dipolar moment. The observed intensity is affected by abundance variations due to complex chemistry, molecular photodissociation, or freezeout in the cool disk mid-plane, as well as high optical depths and uncertain excitation

processes. Unlike the continuum, a more limited number of gas surveys have been carried out. Mid-IR studies of H_2O show emission from the inner 10 AU in many T Tauri but few HAeBe stars (Pontoppidan et al. 2010). Spitzer surveys of [NeII] at 12.8 μm show warm gas in many systems, thought to arise from winds from the disk surface at radii up to ~ 10 AU (Lahuis et al. 2007; Pascucci & Sterzik 2009). At sub-mm wavelengths, limited surveys of low-J rotational lines of CO have been carried out, both with single-dish telescopes (Zuckerman et al. 1995; Dent et al. 2005), and with interferometers (Öberg et al. 2010). Most of this emission arises from 30 to 300 AU radii. In the far-IR, scans of a few bright embedded Class 0 YSOs (e.g., L1448-mm) and massive young stars (e.g., Orion-KL) with the long-wavelength spectrometer (LWS) on ISO showed rich spectra, including fine structure lines of [OI] and [CII], and many transitions of H_2O and CO (Benedettini et al. 2002; van Dishoeck 2004). Class I YSOs also show similar lines, albeit fainter than the Class 0s. Among less embedded systems, the bright ‘prototypical’ Class I–II object T Tauri³² also has many FIR lines (Spinoglio et al. 2000). However, more typical optically-visible Class II–III objects were not detected in FIR lines due to the relatively low sensitivity and large beams.

Both gas and dust observations suffer from problems in interpretation, and both are needed for the best understanding of disks. The motivation for GASPS was to conduct a relatively large, systematic study of gas and dust in the far-infrared, utilising the sensitivity improvements available with the Herschel Space Observatory.³³ The survey covers a broad sample of optically-visible young systems, from Class II gas-rich protoplanetary disks through to Class III objects and gas-poor debris disks. It focusses on the brightest lines and the FIR peak of the continuum emission, and is complemented by data at other wavelengths. In this article, we describe the survey and observing techniques (§ 2), discuss the target selection criteria, and give the complete target list (§ 3 and the Appendix A). Section 4 summarises the origins of FIR line emission in these objects, and outlines the modeling used by GASPS. In § 5 we give an overview of the results, with the lines detected and the detection statistics.

2. THE GASPS SURVEY

GASPS (Gas Survey of Protoplanetary Systems) uses the photodetector Array Camera & Spectrophotometer (PACS) (Poglitsch et al. 2010) on the *Herschel* spacecraft (Pilbratt et al. 2010) to study a predefined set of the brightest lines and dust continuum in the far-infrared from a relatively large sample of targets. The aim was to allow the detection of gas in systems

³²There is some discussion as to whether T Tauri should actually be classified as a Class I YSO with a massive envelope: typically, the prototypical object in a class actually turns out to be rather unusual!

³³*Herschel* is an ESA space observatory with science instruments provided by European-led Principal Investigator consortia and with important participation from NASA.

with a disk mass limit similar to, and possibly lower than, existing sub-mm dust surveys. The wavelength coverage of the spectroscopic observations was tailored to include the [OI] 3P_1 - 3P_2 and 3P_0 - 3P_1 lines at 63 and 145 μm , [CII] $^2P_{3/2}$ - $^2P_{1/2}$ at 157 μm , several H₂O lines, particularly those at 78 and 180 μm , along with adjacent transitions of CO and OH observable without incurring a significant penalty on the total required time. In addition, GASPS provides accurate far-infrared photometry at 70 and 160 μm and, in most cases, 100 μm .³⁴ The project was awarded 400 hr of time to survey up to 250 young systems (in several cases, multiple systems were covered in the same observation), and observations were taken at various times between 2010 December and 2012 July. The spectrometer was used with up to 4 settings per target, each of which covered a relatively small wavelength range (typically $\Delta\lambda/\lambda \sim 5\%$) simultaneously in two PACS grating orders. Most objects were observed in the setting covering the [OI]63 μm line, with a subset of the brighter ones observed in the other settings, resulting in a two-phase survey strategy (see § 2.1.3).

To help maintain the unbiased nature of the survey, targets were chosen with a wide range of spectral type, disk dust mass, age, and other stellar parameters (see § 3). They were located in seven well-studied young clusters and associations, with a distance range of 40–200 pc (with the majority around 150 pc). Assuming typical disk sizes of 100–300 AU (Williams & Cieza 2011) and with the angular resolution of Herschel/PACS of 5" at the shortest wavelength, line and continuum emission from the disk itself is unlikely to be spatially resolved. With the highest spectral resolution of PACS (88 km s⁻¹ at 63 μm), disk emission will also not be spectrally resolved (the Keplerian rotation velocity of most of the disk mass is ~ 10 –50 km s⁻¹). However, nondisk components such as outflow jets or ambient cloud emission may be resolved (see § 4). In most cases, all we have is a single measurement of the line flux on each target, yielding highly degenerate solutions to the underlying disk physics and chemistry. In the absence of resolution, a survey covering a wide range of target parameters is required, along with detailed modeling and data from other wavelengths.

2.1. Observational Technique and Survey Strategy

2.1.1. PACS Spectroscopy

The PACS instrument (Poglitsch et al. 2010) offers resolutions of 1500–3400 (200–88 km s⁻¹) and the ability to observe most of the 60–200 μm wavelength range. In spectroscopic mode, PACS provides an IFU with a 5 × 5 array of spaxels, and a pixel size of 9.2". By comparison, the instrumental point-spread function (PSF) ranges from 4.5" (FWHM) at 63 μm up to 13" at 180 μm . For the GASPS project, spectral observations

³⁴FIR fluxes for the brighter objects are available from IRAS, ISO or Spitzer, although in many cases the fluxes at $\lambda > 70$ are unreliable because of the large beams and confusion levels involved—particularly in star forming regions.

were taken using line-scan or range-scan modes, whereby the grating is scanned over a small wavelength range, taking data from all detector pixels simultaneously. Wavelengths around the central region of the spectra are observed by all of the 16 detector pixels to minimise flat-fielding problems due to inter-pixel variations. Line-scan observations have small wavelength coverage, and are designed to cover a single spectrally-unresolved line and immediately adjacent continuum with the full sensitivity. Range-scan observations have an arbitrary wavelength coverage and for GASPS were set up to include several close lines of interest by scanning up to 2 μm . Table 1 shows the settings of the four wavelength scans A through D. Each has a primary line targetted in one of the grating orders; the secondary simultaneous grating order (given in brackets) was used to observe other useful lines (the full list of lines detected during the course of the survey is given in § 5.1). For a few individual targets, integration times longer than given in Table 1 were used for followup of marginal detections. Note that with the array spectral scanning technique, not all wavelengths are being observed by a detector at all times, so the noise level increases towards the spectrum edges. However, the rms values in the scan centre in Table 1 are in good agreement with predictions. The observed sensitivity at 63 μm is equivalent to a 3σ line luminosity sensitivity limit of $6 \times 10^{-6} (D/140)^2 L_{\odot}$, where D is the source distance in pc.

Observations were performed in chop-nod mode with a small throw (1.5'), primarily to remove telescope and background variations. This chops out smooth background emission from around the source, but it may result in confusion from chopping onto extended emission. In some targets, this could be seen in the [CII] line (§ 4.5).

2.1.2. PACS Photometry

Photometric data were obtained using the fast scanning mode of the PACS imaging photometer, operating at central wavelengths of 70 and 160 μm simultaneously (and repeated at 100 and 160 μm in most objects). This technique scans the telescope over the source, using relatively short scan lengths of 3.5', and small (4") orthogonal steps between each scan. Two scans were performed, at 70° and 110° to the array, to improve the final image fidelity and avoid striping effects in the scan direction. The photometer array field-of-view is 3.5' × 1.75' and, although the resultant image does not have a constant signal-to-noise ratio over the field, the noise level in the central 180" × 80" region varied by less than 20%. The technique was found to be more sensitive than the chop-nod method, and in some cases several objects could be covered in the same field. It also enabled searches for faint companions in the radius range ~ 1500 –7000 AU. The required sensitivity for the photometric observations was better than 5 mJy rms at 100 and 160 μm , and a factor of ~ 2 lower at 70 μm . Although the FIR continuum flux from disks is dependent on the stellar luminosity and mean disk temperature as well as the dust mass (and may be optically

TABLE 1
PACS WAVELENGTH SETTINGS AND SENSITIVITIES IN THE PRIMARY GRATING ORDER

Grating setting	Primary line	Primary λ (μm)	Grating orders	Time ^a (s)	Predicted rms ^b	Observed rms ^b	Notes
A	[OI]63.2	63.08–63.29	3 (1)	1760	4.6	2.5–3	LineScan
B	[CII]157.7	157.10–158.90	1 (2)	1500	1.3	0.8–1.4	RangeScan
C	H ₂ O 180	178.90–181.00	1 (2)	2000	1.7	2.0	RangeScan
D	[OI]145.5	144.00–146.10	1 (2)	1630	1.4	1.6	RangeScan
Phot	(Blue)	60–85	3	180	2.3	2.6–3.0	
Phot	(Green)	85–130	3	180	2.7	2.6–3.0	
Phot	(Red)	130–210	1	360	3.6	4.7–9.0	(Background)

^a Approximate times for most targets in the main survey, not including overheads.

^b Note that noise rms levels are given in units of 10^{-18} W m⁻² for the spectroscopic observations, and in mJy for the continuum photometry.

thick), disks of dust mass 10^{-5} – 10^{-3} M_{\odot} have IRAS 60 μm fluxes of typically 1 Jy at the fiducial distance of 150 pc. So the survey should detect dust in systems 1–2 orders of magnitude fainter than this. The noise level of the observations was generally close to the original prediction (see Table 1), although in some cases it was limited by galactic background emission at 160 μm . Although the spectroscopic data could in principle be used to give narrowband continuum fluxes from the line-free parts of the spectra (albeit with a factor of ~ 30 less sensitivity than the full photometry), it was found that the photometric accuracy of these data was lower than the broad-band photometry, and generally they were not used for SED fitting.

2.1.3. Phased Survey Strategy and Data Reduction

The spectroscopic observations were carried out in one or more of the wavelength settings in Table 1. Phase I of the project consisted of [OI]63 μm observations of most targets using grating setting A, concatenated observations of the brightest $\sim 10\%$ of targets in settings B–D (in order to reduce spacecraft slew overheads), plus photometry.³⁵ Note that not all objects from the initial survey list were observed in the lines; based on early survey results, a number of targets were dropped as they were deemed too faint in continuum to have likely emission in any line. In addition a few Taurus objects were dropped from both continuum and line observing based on updated re-classification as field stars (Luhman et al. 2009). Phase II of the project consisted of flexible followup of the brightest [OI] targets using grating settings B, C and/or D, as well as some deeper observations of a few individual sources.

During the course of the survey, GASPS photometric and spectroscopic data were reduced using prevailing versions of the standard Herschel data processing pipeline, HIPE (Ott 2010). This provides calibrated FITS images and datacubes;

³⁵ Some bright targets were dropped from the photometric list, as suitable data was available from other Herschel surveys, e.g., some of the Taurus and ChaII objects were covered by the Gould Belt Survey.

further photometry and spectroscopic extraction were performed with packages such as STARLINK Gaia. However, the released version of HIPE evolved during the course of the mission and different versions were used to reduce GASPS datasets in different publications, ranging from version 2.3 in early data (Meeus et al. 2010) to version 7.0 (Riviere-Marichalar et al. 2012a) and version 9.0 (Howard et al. 2013, in preparation). Later HIPE releases generally have improved calibration as well as better flat-fielding, and the complete GASPS survey is to be re-reduced using a single mature version before being made publicly available as a systematically-calibrated dataset. The current work makes use of data extracted from the Herschel science archive during 2012, but the detection statistics presented here are unlikely to change significantly in the final data release.

3. TARGET SELECTION

GASPS targets were selected from the seven well-known nearby young star formation regions and associations listed in Table 2 and described in § 3.1. The complete target list, with system parameters from the literature, is given in Appendix A. For completeness, we list all the initial targets in this table, although some were not observed in spectral lines in the final survey (see above). The criteria used to select the targets were:

1. Age range 0.3–30 Myr. As discussed by several authors (e.g., Hartmann et al. 2001), stellar ages are uncertain—particularly for ≥ 10 Myr—and in these cases it may be better to take the ensemble age for a cluster rather than ages of individual stars. Systems of age ≤ 0.3 Myr were considered more likely to include nondisk emission components such as remnant ambient material, infalling envelopes, or energetic outflows (see § 4). Those older than ~ 30 Myr were expected to have very little circumstellar gas.

2. Optically visible stars. This means mostly SED Class II, III, Transition Objects, or debris disks. Targets have optical extinctions less than $\sim 3^m$. We avoided embedded objects (i.e., Class 0–I), because of potential confusion from extended surrounding gas.

TABLE 2
SUMMARY OF CLUSTERS AND ASSOCIATIONS IN GASPS

Group	Distance (pc)	Age (Myr)	Disk fraction ^a (%)	GASPS targets	Notes/Main population
Taurus	140	0.3–4	90	106	Class I–III T Tauri stars
Cha II	178	2–3	75	19	Class II T Tauri stars
η Cha	97	5–9	56	17	T Tauri and debris disks
TW Hya	30–70	8–10	≥ 30	13	T Tauri and debris disks
Upper Sco	145	5/11	20	44	Class II–III T Tauri stars.
β Pic	10–50	10–20	≥ 37	18	Debris disks
Tuc Hor	20–60	30	≥ 26	16	Debris disks
HAeBe stars	20–200	~ 0.5 –30	100	24	Includes debris disks

^aNote: Disk fractions are based on published photometric excesses. They are the fraction of stars with any measured disk, so include mostly debris disks in the older associations and protoplanetary disks in the younger star forming regions.

3. Disk *dust* masses³⁶ mostly in the range $10^{-3} \leq M_d \leq 10^{-7} M_{\odot}$. Also included were a number of coeval stars with Class III SEDs, or upper limits for M_d of $\sim 10^{-6} M_{\odot}$, where the lack of continuum excesses in the IR or sub-mm suggested negligible warm or cool dust. Some of these still had gas accretion signatures and were included as they potentially could be associated with moderate masses of gas. In addition a number of debris disks in young associations were also observed, with M_d as low as $10^{-11} M_{\odot}$.

4. Stellar spectral type A0 through M5. A similar range of stellar spectral types was chosen in each region where possible, although to increase the numbers of early spectral type objects, we also identified a sample of isolated well-studied Herbig AeBe stars with a similar age spread to that of the clusters. The resulting stellar mass range was ~ 0.2 – $3 M_{\odot}$, based on published HR diagrams.

5. Nearby regions, with distances of < 180 pc for low-mass and < 200 pc for HAeBe stars.

6. Low confusion level (from Herschel Confusion Noise Estimator). Confusion noise was < 100 mJy at $100 \mu\text{m}$. This meant that several dense star-forming regions such as ρ Ophiuchus were excluded from the survey.

7. Extensive photometric and, in many cases, spectroscopic datasets available at other wavelengths.

8. A range of accretion rates (based initially on $H\alpha$ equivalent width, EW), X-ray luminosity, and binary separation.

3.1. Individual Associations

3.1.1. Taurus

The Taurus star formation complex lies at 140 pc with a depth along the line of sight of ~ 20 pc (Torres et al. 2009). Taurus contains mostly low-mass stars with an age range of < 0.1 up to ~ 10 Myr (Palla & Stahler 2002; Güdel et al. 2010).

³⁶ Values of M_d were mostly based on published mm wavelength continuum observations, with estimates based on shorter wavelength data in some cases.

Stars in this region have been extensively studied at many wavelengths, and the census of Class 0–II YSOs is essentially complete, with a significant fraction of the Class III YSOs also known (Rebull et al. 2010). Stellar parameters in Appendix A are from Kenyon & Hartmann (1995) and Kenyon et al. (1998), updated where appropriate by values in Furlan et al. (2006), Güdel et al. (2007) and Rebull et al. (2010), and with disk masses from Andrews & Williams (2005) and Currie & Sicilia-Aguilar (2011).

3.1.2. Cha II

Chamaeleon II is a nearby (178 pc; Whittet et al. 1997) star forming region included in the Spitzer Legacy cores-to-disks program (Evans et al. 2009) and the Gould Belt key program (André et al. 2010). It contains a lightly clustered distribution of low mass YSOs in a range of evolutionary states with spectral types K–M and ages estimated from protostellar evolutionary tracks of 4 ± 2 Myr (Spezzi et al. 2008). The GASPS subsample consists of 19 targets from Cha II, generally with infrared colors of Class II objects and/or $H\alpha$ equivalent widths indicative of gas accretion. Although there exists no deep sub-mm survey to give disk mass estimates (the survey of Young et al. [2005] only detected DK Cha and possibly IRAS12500-7658, with a dust mass limit on the other objects of $2 \times 10^{-4} M_{\odot}$), Alcalá et al. (2008) have estimated masses based on SED fits to far-IR data, and so we give these values (using their D01 models) in Appendix A. However, it should be noted that these entail higher uncertainties compared with estimates from the sub-mm. Spectral types are from Spezzi et al. (2008), binarity is discussed in Alcalá et al. (2008), and L_x comes from the ROSAT survey of Alcalá et al. (2000).

3.1.3. Upper Sco

The mean cluster age and distance of Upper Sco was estimated as 5 Myr and 145 pc by de Zeeuw et al. (1999), although more recent estimates suggest it may be as old as 11 Myr (Pecaut et al. 2012), which is consistent with the rather low disk

fraction observed. The 8–70 μm SED has been used to identify disks as Class II, Class III, or debris (Carpenter et al. 2009), and these classifications are given in Appendix A. The disk masses and system parameters are from the sub-mm observations of Mathews et al. (2012) and references therein.

3.1.4. η Cha

This is a compact grouping of ~ 19 stars, first identified as a young association through X-ray observations (Mamajek et al. 1999). One of the reasons for interest in this cluster is its age, at an estimated 8 Myr, and relatively close distance (97 pc). The disk fraction, based on Spitzer observations at 24 and 70 μm (Gautier et al. 2008), is 56%, which is relatively large for the age of the association (c.f., Haisch et al. 2001). A number of the stars are active accretors, and at least two are identified as Class II T Tauri stars (Sicilia-Aguilar et al. 2009). In the target list, spectral types, H α EW, and the presence of an infrared excess are based on Sicilia-Aguilar et al. (2009), and information on binarity is from Bouwman et al. (2006). X-ray luminosities are taken from Mamajek et al. (1999) and López-Santiago et al. (2010), and disk mass estimates are mostly based on FIR measurements (Currie & Sicilia-Aguilar 2011).

3.1.5. TW Hya Association

First recognised as a group of nearby young stars by Kastner et al. (1997), the number of members in the TW Hya association (TWA) is now at least 25 (Webb et al. 1999; Mamajek 2005). It is the closest association with accreting T Tauri stars, and includes two classical T Tauri stars (TW Hya itself, and Hen 3-600), and two bright debris disks (HD 98800, a hierarchical multiple system, and HR4796A). Low et al. (2005) used Spitzer to measure 24 and 70 μm excesses around TWA members and found these four systems have a 24 μm excess a factor of ~ 100 larger than the other members. However, several of the other stars also have evidence of dust disks, from weak excesses at longer wavelengths. The age of this system is confirmed at ~ 10 Myr (Barrado Y Navascués 2006). Parameters in Appendix A are taken from de la Reza & Pinzón (2004) and Scholz et al. (2007), with disk masses mostly from Mathews et al. (2007). Note that TWA member HR4796A (TWA11) is listed under the HAeBe stars as A-12.

3.1.6. β Pic

The moving group associated with β Pic was identified by Barrado y Navascués et al. (1999), and membership extended by Zuckerman et al. (2001) and others (see Torres et al. [2008] for a summary). With a derived mean age of 12 Myr, and range in distance of 10–50 pc, many of its members have been extensively studied over a wide range of wavelengths, including 24 and 70 μm with Spitzer (Rebull et al. 2008), as well as the submm (Nilsson et al. 2009). The disk fraction is $\geq 37\%$ (Rebull et al. 2008), and includes a number of debris disks in addition to

β Pic itself.³⁷ Data in Appendix A are mostly from the above references. Detailed results from GASPS, including model fits to the photometry, have been presented for HD 181327, one of the brightest debris disks in this group, and HD 172555 (Lebreton et al. 2012; Riviere-Marichalar et al. 2012b).

3.1.7. TucHor

This stellar association was first recognised by Zuckerman & Webb (2000) and Torres et al. (2000), who derived an age of 20–40 Myr and distance range of 20–60 pc. No N-band excesses were seen around any stars in Tuc Hor (Mamajek et al. 2004). However, a Spitzer study at 24 and 70 μm (Smith et al. 2006) showed 5/21 stars with a measurable excess at 70 μm . Zuckerman et al. (2011) subsequently extended the search and found several more stars with IR excesses. All such systems in Tuc Hor are thought to be debris disks, and this is the oldest association in GASPS. The photometric data have been presented in Donaldson et al. (2012).

3.1.8. Herbig Ae Be stars

The survey includes 25 IR-excess stars of spectral types late B to F, improving the statistics at the higher end of the stellar mass range (around 2–4 M_{\odot}).³⁸ This sample also includes some A-type stars with excesses where the classification is less clear: the peculiar Be star 51 Oph (Thi et al. 2005), and 5 systems which may be classified as debris or HAe (including 49 Cet, where the age was recently revised to 40 Myr [Zuckerman & Song 2012]). Like the lower-mass counterparts, the program HAeBe stars are biased toward isolated systems which have published IR excesses and ancillary data (particularly UV spectra, resolved coronagraphic images and/or millimeter interferometry). HD 97048—one of the brightest targets in our sample—had prior evidence from ISO of [OI] and possibly [CII] emission (Lorenzetti et al. 1999). The HAe sample includes several disks with large gaps and/or cavities, as well as 2–3 systems with jets. Unlike the T Tauri stars, which are represented in sufficient number to permit statistical evaluation of association ages, the HAe stars represent extremes in stellar and disk properties, and have more uncertain ages except where there are common proper motion late-type companions. Stellar parameters in Appendix A are mostly taken from Montesinos et al. (2009) and Meeus et al. (2012), with disk masses from Acke et al. (2004) and Sandell et al. (2011). Note that the SED classifications in the appendix are different from the T Tauri class, and are based on the mid-IR slope as suggested by Meeus et al. (2001): Group I has an SED rising to longer wavelengths in the mid-IR, and group II has a falling SED. Results from the GASPS HAeBe subsample have been presented in Meeus et al. (2012).

³⁷ β Pic was observed as part of the Herschel GT Program ‘Stellar Disk Evolution’ (P.I. G. Olofsson).

³⁸ Note that the HAe star AB Aur is listed under the Taurus subsample as T-101 in Appendix A.

3.2. Ancillary Data

Many of the GASPS targets are well-known systems, with photometry in optical through to mid-IR (including Spitzer fluxes at wavelengths as long as $70\ \mu\text{m}$), and sub-mm (mostly $850\ \mu\text{m}$). In addition, $\text{H}\alpha$ or $\text{Br}\gamma$ line strengths are published for many targets. Derived parameters such as stellar spectral type, T_{eff} , disk dust mass, and SED Class are also mostly available, and the most recent published estimates are given in Appendix A. As part of the GASPS project, we have endeavoured to obtain such data in cases where it is missing, and to make the target sample uniform both in data and in derived parameters. One additional issue is that much of the published photometry is not contemporaneous; in some cases, photometric points in the optical and NIR have been taken 20 years apart. For time-variable objects, SED fitting under these circumstances may be significantly affected, and more recent optical and near-IR photometry is being obtained for a number of the targets in order to improve the reliability of SED fits.

4. ORIGINS OF FAR INFRARED LINES FROM YOUNG STARS

At far-infrared wavelengths, common species such as C, O and N have several prominent fine-structure transitions. [OI] lines at 63 and $145\ \mu\text{m}$ and the [CII] line at $157\ \mu\text{m}$ are important cloud coolants, on a galactic scale (Stacey et al. 1991), in photodissociation regions (Hollenbach et al. 1991), and in circumstellar disks (Kamp et al. 2003; Gorti & Hollenbach 2004). In star formation regions, both models and observations indicate that [OI]63 μm is the single brightest emission line in the FIR/sub-mm. Abundant molecules such as CO and H_2O also have numerous rotational lines throughout the FIR with energy levels of a few hundred K, and can trace the ‘warm’ gas components. Other FIR-emitting species such as OH are photodissociation products of H_2O , and are therefore predicted to be abundant (Najita et al. 2010). Around individual young stars, FIR lines can arise from several different regions. For example, CO and OH emission from young highly luminous HAeBe stars was thought to arise from dense regions of size $\sim 200\ \text{AU}$ (Giannini et al. 1999), but it was unclear whether these were disks or remnant envelopes. Lines are also seen from high-velocity jets and low-velocity photoevaporating disk winds, and the relative contributions of disk, outflow, disk wind, and envelope will depend on the SED class, stellar radiation field, disk structure, mass loss rate and the environment.

The GASPS project involves both in-depth studies of individual targets using multi-wavelength data, as well as a statistical analysis of the full FIR sample. Interpretation of the results generally requires detailed comparison with models, and in the following sections we outline methods of estimating the contributions to the FIR line emission, focussing on Class II–III YSOs, which form the bulk of our targets.

4.1. Disks

Fine structure atomic line emission arises from the surface of disks at $A_V \sim 1$ over a wide range of radii, where the stellar UV or X-ray photons ionise the exposed gas to produce a mainly atomic extended disk atmosphere (Meijerink et al. 2008; Gorti & Hollenbach 2008; Woitke et al. 2009a). [OI]63 μm is predicted to be the brightest line from disks at any wavelength, with line luminosities as high as $\sim 10^{-4} L_\odot$ from T Tauri systems (Gorti & Hollenbach, 2008). It becomes optically thick relatively easily, and traces the mean gas temperature on the disk surface rather than the mass directly. FIR molecular lines such as CO and H_2O also arise from the warm heated surface of dense disks (Woitke et al. 2009b). However, molecular photodissociation in more tenuous debris disk systems may mean the atomic fine structure lines will dominate the FIR (Kamp et al. 2003; Zagorovsky et al. 2010). Line fluxes depend strongly on the disk structure (for example, a flared disk has a larger exposed surface area, resulting in brighter lines [Jonkheid et al. 2004]), the radiation field from the central star, as well as the details of chemistry and gas/dust ratio in the disk atmosphere. In the following we summarise the methods used for modeling the data.

4.1.1. Disk Modeling

MCFOST and **ProDiMo** are the two main codes used in GASPS to model the protoplanetary disk structure and appearance. **MCFOST** is a three-dimensional Monte Carlo continuum and line radiative transfer code (Pinte et al. 2006, 2009). The parametrized input disk density distributions can accommodate structures such as holes, gaps and dust settling. The calculation of the dust temperature and radiation field takes into account non-isotropic scattering, absorption and re-emission based on the local dust properties. The code uses a large variety of grain size distributions and compositions, e.g., porous grains and icy grains. SEDs, thermal and scattered light images, visibilities, as well as line emission are derived by a Monte-Carlo method and ray-tracing of the final physical disk structure. **ProDiMo** is a two-dimensional thermo-chemical disk code that calculates the vertical hydrostatic equilibrium, gas phase (e.g., neutral-neutral, ion-molecule, photochemistry, X-ray chemistry), and gas-grain chemistry (ad- and desorption processes), two-dimensional continuum radiative transfer (with isotropic scattering), detailed gas heating/cooling processes (including X-rays) using 2-directional escape probability, and spatial decoupling of gas and dust (e.g., settling) (Woitke et al. 2009a; Kamp et al. 2010; Aresu et al. 2011; Woitke et al. 2011). The observables derived from the resulting chemo-physical disk structure include SEDs, line fluxes, profiles, and images. For optically thin cases such as debris disks, we also use **GRaTer**, a ray-tracing code incorporating a large variety of grain compositions which fits SEDs, images, and interferometric visibilities using parametrized optically thin disk models (Augereau et al. 1999).

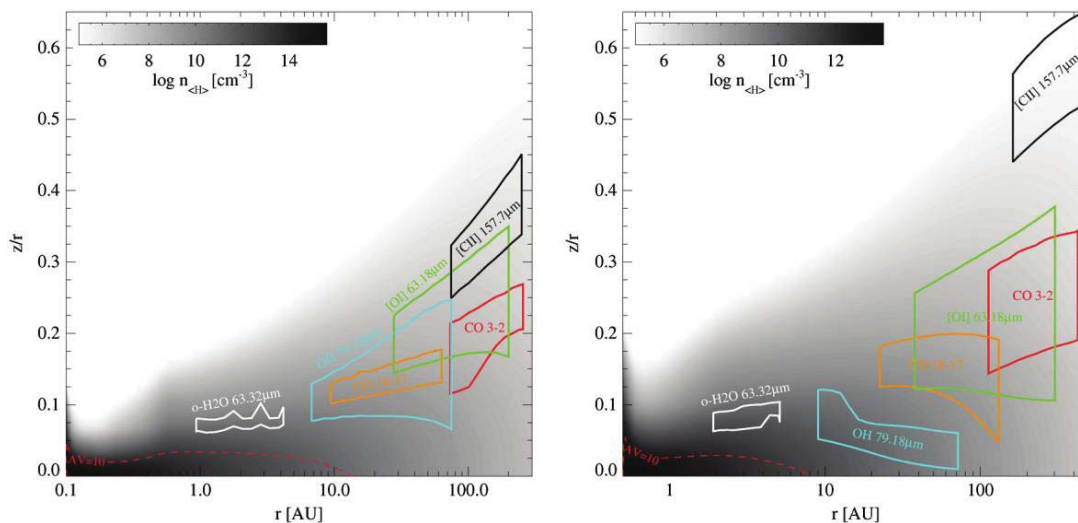


FIG. 1.—Cross-sections through ProDiMo models of a T Tauri disk (*left*) and a HAeBe disk (*right*), with the density structure as a greyscale, and the $A_V = 10^m$ surface shown as a *dashed red line*. The primary emitting regions for GASPS lines are given by the coloured boxes, and indicate where 80% of the emission arises. The lines are [OI]63 μm (green), CO $J = 18 - 17$ (orange), [CII]157 μm (black), OH79 μm (blue) and the 63.3 μm H₂O line (white). Also shown is the CO $J = 3 - 2$ emitting region (red). Model parameters are given in Table 3. Note the larger outer radius displayed in the HAeBe model.

For modeling individual sources, grids of **MCFOST** or **GRaTer** models were run over a broad parameter space to identify the best fitting dust model, based on SEDs, images, and interferometric data when available. **MCFOST** results were passed to **ProDiMo** for detailed gas modeling. Examples of this approach are Meeus et al. (2010) and Thi et al. (2010) and for a debris disk, Lebreton et al. (2012). Another approach employs a genetic algorithm minimisation strategy with the **ProDiMo** models to find local minima in the parameter space constrained by observations. Examples are found in Tilling et al. (2012) and Woitke et al. (2011).

In Figure 1 we use **ProDiMo** to illustrate the regions where most FIR line emission is expected to arise in T Tauri and HAeBe disks, using the model parameters given in Table 3. Note that these are relatively massive disks—towards the high end of the range of the GASPS sample. For these models we have proscribed the disk vertical structure by the scale height and flaring index. The results indicate that the [OI] lines are seen mostly from the disk surface at 20–200 AU radius around a T Tauri star, and a factor of 1.5 further out in the more luminous HAeBe star. The [CII] line comes from the tenuous outer atmosphere at radii >100 AU, whereas high- J CO emission (e.g., the $J = 18 - 17$ line at 144.78 μm) is predicted to arise only from within a few tens of AU for T Tauri disks. The model predicts emission from the 63.3 μm line of H₂O mostly from within a few AU.

4.1.2. Model Grids

To support a broader statistical analysis of the GASPS data, we have produced a grid of models covering a wide parameter

space (Woitke et al. 2010).³⁹ Stellar masses between 0.5 and 2.5 M_\odot and pre-main sequence evolutionary tracks at 1, 3, 10, and 100 Myr are used to define T_{eff} , R_* and hence L_* . The UV excess, f_{UV} , is treated as a power-law that is added on top of the photospheric spectrum in the wavelength range 912–2500 \AA . Dust masses range from 10^{-7} to $10^{-3} M_\odot$, and the gas/dust mass ratio runs from 10^3 ($10 \times \text{ISM}$) to 0.1 ($0.001 \times \text{ISM}$). Geometries include young flaring disks, flat evolved systems, as well as ‘transition’ disks with inner holes up to 100 times the sublimation radius. The grid also contains models with a settled dust distribution, where larger grains have a smaller vertical scale height than smaller ones. The observables calculated from these models include SEDs and integrated line fluxes.

Woitke et al. (2010) show that the fine structure line fluxes of [OI] and [CII] depend strongly on the stellar UV excess and disk flaring. Using the entire grid of parameter space (not folding in the likelihood of these disks occurring in nature), about 70% of the high-mass models (dust mass, $M_d \geq 10^{-5} M_\odot$) with a strong UV excess were predicted to be detected in [OI]63 μm line by GASPS, and 55% detected in [CII]157 μm . Without a UV excess, the percentage drops to $\sim 30\%$ (14% for [CII]). An initial statistical comparison between the early GASPS line fluxes and the grid (Pinte et al. 2010) shows that some of the disks around low-mass stars ($\lesssim 2 L_\odot$) do require additional heating from a moderate UV excess (with $f_{\text{UV}} = 0.1$) or X-rays (which were not included in this first grid). However, results

³⁹ The grid was calculated on the FOSTINO computer cluster financed by ANR and operated by SCCI at OSUG.

TABLE 3
PARAMETERS USED BY PRODiMO TO ILLUSTRATE THE REGION OF LINE
EMISSION FROM DISKS AROUND T TAURI AND HAEBe STARS IN FIG. 1

Parameter	T Tauri	HAEBe	Notes
SpT	K4	A3	
M_* (M_\odot)	1.4	2.2	
T_{eff} (K)	4500	8600	
L_* (L_\odot)	2.0	32.0	
T (Myr)	2.3	4.6	Age
f_{UV}	0.01	0	Additional UV fraction, L_{UV}/L_*
L_X (erg/s)	10^{30}	0	Additional X-ray luminosity
R_{in} (AU)	0.1	0.5	Set by the grain sublimation radius
R_{out} (AU)	300	500	Outer disk radius
M_d (M_\odot)	10^{-4}	10^{-4}	Disk dust mass
g/d	100	100	Gas/dust mass ratio
ϵ_d	1.0	1.0	Surface density power law exponent
$a_{\text{min}}/a_{\text{max}}$ (μm)	0.05/1000	0.05/1000	Min/max grain size
p	3.5	3.5	Grain size power law
f_{PAH}	0.01	0.01	PAH mass fraction
H_0 (AU)	10	10	Scale height at 100 AU radius
β	1.1	1.1	Disk flaring index

from T Tauri disk modeling with stellar X-rays indicate that the [OI]63 μm line flux is only affected by X-ray heating for $L_X \gtrsim 10^{30}$ erg/s (Aresu et al. 2011).

Although most gas emission lines sample a thin, warm surface layer (see Fig. 1), combining the FIR data with results from other wavelengths (e.g., the [OI]63 μm /CO(2-1) ratio) and with physically-plausible models does allow us to break model degeneracies, giving approximate estimates for gas parameters independent of the dust (Kamp et al. 2011). But it is clear that the reliability of derived values such as the gas mass relies on the accuracy of the models.

4.2. Outflow Jets

Highly embedded Class 0–I YSOs are known to have prominent outflows, and early observations using the KAO as well as more recent observations with Herschel/PACS show bright FIR lines around Herbig-Haro objects and high-velocity CO outflow lobes (Cohen et al. 1988; van Kempen et al. 2010). As well as fine structure lines such as [OI]63 μm , many CO and H₂O transitions are readily detectable from Class 0–I objects (Lorenzetti et al. 2000; Molinari et al. 2000; van Dishoeck 2004; Goicoechea et al. 2012). The stars are young (≤ 0.1 Myr), optically obscured, embedded in an envelope, and located near dense cloud cores. Their dense environments and high outflow luminosities suggest that the FIR line emission is dominated by outflow shocks (Molinari et al. 2000; Nisini et al. 2000, 2002; Franklin et al. 2008). These shocks also affect molecular

abundances; for example, releasing H₂O from grains and increasing its gas-phase abundance to as much as 10^{-4} —comparable with that of CO (Benedettini et al. 2002). In most cases the FIR lines dominate the shock cooling, and line fluxes may be used to estimate the outflow luminosity (Hollenbach et al. 1985; Nisini et al. 2002; Podio et al. 2012).

Evolved, isolated objects such as optically-visible Class II–III T Tauri stars have mass accretion rates at least 1–2 orders of magnitude lower than Class I objects (Hartmann et al. 1998; Arce & Sargent 2006), which are themselves an order of magnitude lower than the Class 0 objects (Bontemps et al. 1996; Podio et al. 2012). Class II objects are pure disk systems, and are generally isolated with no dense ambient gas. Consequently we assume the fraction of outflow luminosity deposited in shocks near the star, η_s , is given by the geometric fraction of the initially broad wind intercepted by the disk. So $\eta_s \sim H_0/100$, where H_0 is the scale height (in AU) at 100 AU radius. In the same way as embedded objects, the jet mass loss rate \dot{M}_{out} can be estimated from the [OI]63 μm luminosity, L_{OI} by:

$$\dot{M}_{\text{out}} = 2 \cdot L_{\text{OI}} / [v_w^2 \cdot f_{\text{OI}} \cdot \eta_s \cdot (v_a/v_w)],$$

where f_{OI} is the fraction of FIR line luminosity in the [OI]63 μm line, v_w the outflow jet velocity, and v_a the ambient shock velocity (Nisini et al. 2002). For embedded objects, the dominant emission is from the integrated CO and H₂O lines, thought to be from C shocks, and Goicoechea et al. (2012) find $f_{\text{OI}} \sim 0.12$ in the Class 0 YSO Serpens SMM1. In fast dissociative J shocks, [OI]63 μm emission may dominate the luminosity, and f_{OI} is found to be 0.5 or greater (Podio et al. 2012). Assuming a jet velocity of 100 km s^{-1} (Podio et al. 2012), $v_a/v_w = 0.2$ (Nisini et al. 2002), with $H_0 = 10$ AU (Table 3), then the GASPS sensitivity (§ 2.1.1) may allow the detection of outflow mass loss rates of $\sim 3 \times 10^{-9} M_\odot/\text{yr}$ for stars at a distance of 140 pc. However, if C shocks dominate, the contribution to the [OI] line from the jet may be lower. In Appendix A we have indicated the stars with published mass loss rates greater than this value (Hartigan et al. 1995).

Although most are isolated disks, a few of the GASPS targets are somewhat embedded Class II objects and have extended optical jets; for these we may expect some outflow contribution to the FIR lines. The spatial resolution of PACS is modest, but can help investigate this contribution, resolving jets on scales of >1000 AU. For spatially-unresolved outflows the situation is less clear. However, shocked outflow emission may be broadened to $\sim 200 \text{ km s}^{-1}$ or velocity-shifted by more than a few tens of km s^{-1} , similar to the high-velocity component seen in optical lines in a few high-accretion objects (Hartigan et al. 1995; Acke et al. 2005). In these cases, the PACS spectral resolution of 88 km s^{-1} at 63 μm may also be used to help discriminate between outflow and disk.

4.3. Remnant Envelope Gas

Low-density PDRs in the remnant envelope gas centred on the stars may contribute to the [CII] flux from some objects, as the [CII]157 μm critical density is only $\sim 3 \times 10^3 \text{ cm}^{-3}$. To mitigate this, targets were selected to be SED Class II–III with low A_V , i.e., optically-visible stars where the envelope mass is at least 1 or 2 orders of magnitude less than the disk mass (Fuente et al. 2002; Arce & Sargent 2006). The [OI]63 μm critical density is ~ 100 times higher than [CII], and the mean envelope density is small compared to the disk, so the envelope contribution to the total [OI] flux should be small.

4.4. Disk Winds

A photoevaporative UV-driven wind (Pascucci & Sterzik 2009) will serve to extend the scale height of a disk atmosphere, and may enhance FIR emission lines. The effect of this on the [OI]63 μm flux is under investigation.

4.5. Extended Ambient Gas

Observations of star-forming clouds in FIR fine structure lines using the LWS on ISO showed bright emission in regions containing luminous Herbig AeBe and FU Ori stars (Lorenzetti et al. 1999, 2000; Creech-Eakman et al. 2002). The [CII] emission in many of these objects was spatially extended, and commonly the line fluxes at reference positions many arcminutes from the stars were as bright as the on-source position. In these cases, the dominant [CII] source was thought to be extended low-density PDRs, with optical depths of $1\text{--}2^m$ (Hollenbach & Tielens 1997). The GASPS targets were chosen to avoid the densest clouds, and we used the Herschel Confusion Noise Estimator (HCNE) to estimate the 100 μm continuum confusion noise (F_c) for all targets. From this we estimate a [CII] confusion noise level by adopting a ratio of $I_{\text{[CII]}}/F_c = 1.2 \times 10^{-19} \text{ W m}^{-2}/\text{mJy}$, found for large-scale Galactic clouds by Shibai et al. (1991). During the course of the survey, 10 objects having a relatively high continuum confusion level ($F_c > 30 \text{ mJy}$) were observed in [CII] (8 of which were in the Taurus cloud). Based on the HCNE, the predicted [CII] confusion level for these was $> 3.6 \times 10^{-18} \text{ W m}^{-2}$. An examination of the initial data shows no extended [CII] over the PACS footprint in 9 of these objects, with an rms level of $\sim 2 \times 10^{-18} \text{ W m}^{-2}$. Either the confusion level is lower than predictions from the HCNE, or the [CII] emission is smooth over the PACS IFU field ($\sim \text{arcmin}$) and emission is being chopped out. One high background confusion source (HD 163296) had evidence of extended [CII] at a level of $\sim 10^{-17} \text{ W m}^{-2}$ in the PACS field of view and in the chopped reference beam. From the HCNE, this object has the highest value of F_c in the GASPS sample (85 mJy), which would predict, based on the above ratio, a [CII] confusion noise of $I_{\text{[CII]}} = 10^{-17} \text{ W m}^{-2}$, consistent with the observations.

The $100\times$ larger critical density of [OI]63 μm compared with [CII] implies that extended [OI] emission from diffuse ambient

gas is expected to be negligible (Liseau et al. 2006). ISO found that the 63 μm line flux is mostly higher towards highly luminous YSOs than off-source.

4.5.1. Line-of-Sight Absorption

As well as emission, dense clouds may have significant optical depth and be self-absorbed in the [OI]63 line. However, estimates suggest the line optical depth may not become significant until $A_V > 10$ (Liseau et al. 2006; Abel et al. 2007). Moreover, the linewidths of the cool line-of-sight clouds are $< 1 \text{ km s}^{-1}$, small by comparison with the $5\text{--}20 \text{ km s}^{-1}$ widths predicted for Keplerian disk emission. Combined with the extinction limit of $A_V < 3$ in the GASPS survey means this effect should be small in most cases.

5. FIRST RESULTS

Results from some subsets of the GASPS study have been presented in previous papers. A summary of the ‘science demonstration’ observations of a small number of targets was given in Mathews et al. (2010), and a comparison of these data with a broad grid of disk models was shown by Pinte et al. (2010). More detailed comparisons of the line and continuum data with individual tailored models were carried out based on the detections of [OI]63 μm in the T Tauri star TW Hya (Thi et al. 2010) and the HAeBe stars HD 169142 (Meeus et al. 2010) and HD 163296 (Tilling et al. 2012). The T Tauri star ET Cha was detected in both [OI]63 μm and FIR continuum, and modeling indicates the disk is unusually compact (Woitke et al. 2011). CH^+ was detected in one of the brightest targets—the HAeBe system HD 100546 (Thi et al. 2011). An emission line of H_2O at 63.3 μm found in a number of the T Tauri stars indicates warm ($\sim 500 \text{ K}$) H_2O , possibly from the inner few AU of the disks (Riviere-Marichalar et al. 2012a). In most of the older gas-poor systems the lines were not detected; however, the far-IR photometry has been used to improve the SEDs and dust modeling (Donaldson et al. 2012; Lebreton et al. 2012).

In the following sections we summarise some of the overall results from GASPS, including identification of the lines found in the survey, and an initial comparison of the spectra of different types of objects (§ 5.1). In Appendix A (column 12) we indicate which of the four primary lines ([OI]63 μm , [CII]157 μm , CO $J = 18 - 17$, and H_2O) were observed and detected in the targets. For these purposes, a detection is regarded as $> 3\text{-}\sigma$ above the noise. In § 5.2 we give the overall line detection statistics from the survey, and discuss the [OI]63 μm and [CII] emission characteristics in § 5.3 and 5.4. Finally, in § 5.5, we show the effects of other system parameters on the line detection statistics. It should be noted that these data are mostly based on results from early versions of the reduction pipeline HIPE. Consequently, the flux calibration and flat-fielding is not finalised and some detections are subject to re-analysis. Final values of

the fully-calibrated fluxes and detailed flux correlations will be given in subsequent papers.

5.1. Summary of Lines Detected

To illustrate and compare the lines detected in the richer GASPS targets, spectra from the central spaxel in three objects from the survey are shown in Figures 2–5 (note that the spectra are scaled to enable comparison in these figures). T Tau (Podio et al. 2012) (*shown in red*) is a K0V star with a massive disk, compact outflow, some surrounding reflection nebula, and possibly a PDR. FIR lines may arise from a mixture of these components, although the molecular transitions seen in the ISO LWS spectra were attributed mainly to shock emission (Spinoglio et al. 2000). HD 100546 (Meeus et al. 2012) (*shown in blue*) is a young Herbig AeBe star with a bright disk but without a prominent outflow, but which also has a rich FIR spectrum. AA Tau (*in green*) is perhaps a more typical isolated T Tauri star, with a luminosity of $\sim 1 L_{\odot}$, weak outflow and a relatively massive disk. In Table 4 we identify all the lines observed in these three objects.

Both T Tau and HD 100546 have similar strengths in the fine-structure atomic lines. AA Tau is ~ 200 times weaker, but is detected in [OI] with a comparable line/continuum ratio to the others. However, it shows no evidence of [CII]. In HD 100546,

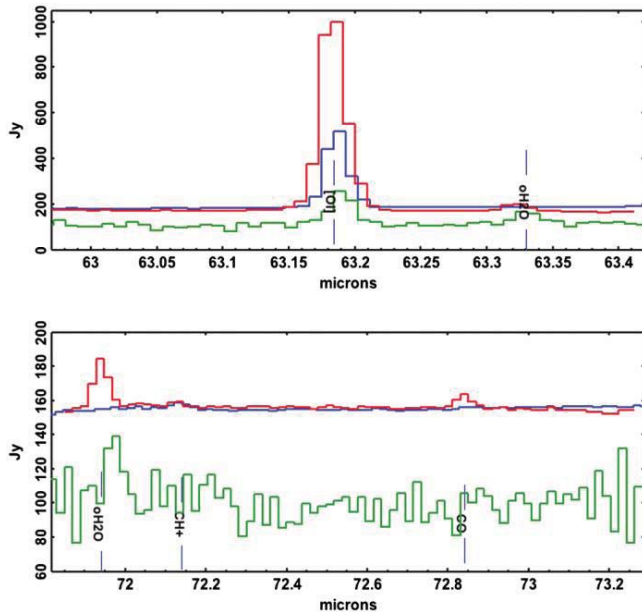


FIG. 2.—Spectra of HD 100546 (*blue*), T Tau (*red*) and AA Tau (*green*), taken from the central PACS spaxel in the two shortest wavelength observations. Fluxes of T Tau and AA Tau fluxes are scaled by 2 and 150 respectively to facilitate comparison of the spectra. Lines found in any of the datasets are identified (although not all the lines are seen in all objects)—see Table 4 for full details of the transitions. Note that small wavelength errors are sometimes apparent in these early reductions of the AA Tau spectra.

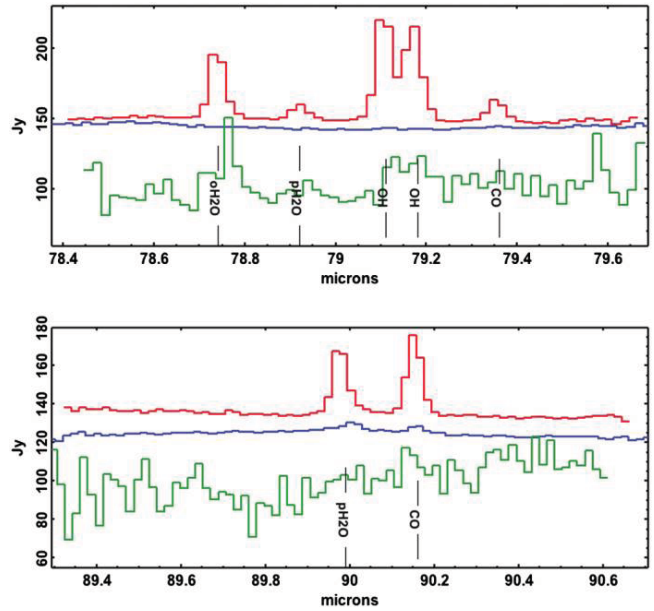


FIG. 3.—Same as Fig. 2, for regions around 79 and 90 μm . The spectra of T Tau and AA Tau have been multiplied by 2 and 150. The emission close to 90 μm is a blend of H_2O and CH^+ , and in HD 100546 is thought to be mostly from CH^+ .

molecular transitions have a line/continuum ratio which is considerably lower than both T Tau and AA Tau. The PACS data cover four transitions of CO: $J = 18 - 17, 29 - 28, 33 - 32$ and

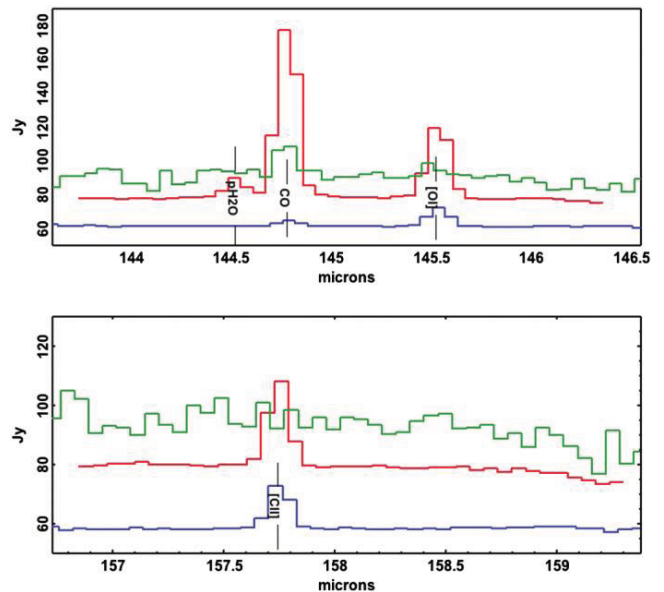


FIG. 4.—Same as Fig. 2 for regions around 145 and 158 μm . The spectra of T Tau and AA Tau have been multiplied by 2 and 150.

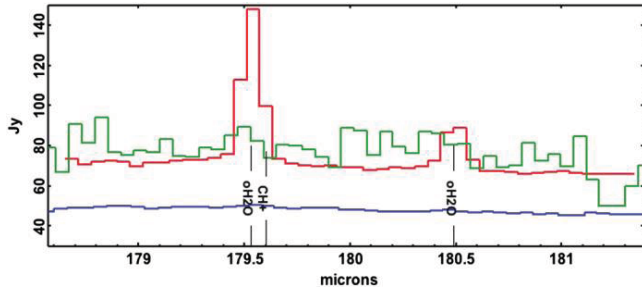


FIG. 5.—Same as Fig. 2 for region around 180 μm . The spectra of T Tau and AA Tau have been multiplied by 2 and 150.

36–35. T Tau shows emission in all four CO lines, and comparison with the CO rotational diagram of Spinoglio et al. (2000) shows that the three highest transitions are new detections, requiring an additional hot gas component (>1000 K) to account for the emission. AA Tau is detected only in the two lower-level CO lines, most likely because of sensitivity limits.

The OH doublet around 79 μm is detected in all three sources (Fig. 3). Several H₂O lines with upper energy levels from 115 to 1300 K are seen towards both T Tau and AA Tau, and in AA Tau, H₂O is the only line detected, other than [OI]63 μm , CO and OH. By contrast, HD100546 has no clear evidence of H₂O emission, although other lines (atomic species, OH and CH⁺) are relatively bright. The highest energy level H₂O transition covered by GASPS is the ortho 8₁₈–7₀₇ line at 63.3 μm (Fig. 2); this was detected in T Tau, AA Tau and several other T Tauri

stars (Riviere-Marichalar et al. 2012a)). Finally, both HD 100546 and T Tauri show clear CH⁺ emission at 72.14 μm , with possible blends of CH⁺ and H₂O around 90.0 and 179.5 μm ; this species was also identified at several other wavelengths in HD 100546 (Thi et al. 2011).

5.2. Primary Line Detection Statistics

Column 12 of Appendix A shows whether each of the four primary species ([OI]63 μm , [CII]157 μm , CO $J = 18 - 17$ and H₂O 63.3 μm) were detected in the GASPS targets. Based on this, the overall detection statistics are given in Table 5. As noted above, observations of the range-scan observations were normally only performed if a target was already found or expected to be detected in [OI]63 μm , so the detection rates of [OI]145 μm , [CII], and CO in this table are biased towards those with known [OI]63 μm emission. Of targets observed in multiple lines, only one remained undetected in [OI]63 μm yet shows emission in one of the other lines. Based on this result and our modeling, it is thought unlikely that a significant number of the [OI]-unobserved objects would show emission in these other lines. The H₂O rates are the fraction of targets seen at 63.3 μm , which was observed as part of the [OI]63 μm line-scan observations. The CO rates are the fraction of targets detected in the brightest line covered by GASPS (CO $J = 18 - 17$).

The main similarities and differences between line emission from the two types of objects are:

1. Of the sample of 164 objects observed in spectroscopy at 63 μm , approximately 49% were detected in [OI].

TABLE 4
LINES IDENTIFIED IN HD100546, T TAU AND/OR AA TAU

Wavelength (μm)	Line ID	Transition	E_{upper} (K)	HD100546	T Tau	AA Tau
63.18	[OI]	3P1-3P2	228	X	X	X
63.33	o-H ₂ O	8 ₁₈ - 7 ₀₇	1293	...	X	X
71.94	o-H ₂ O	7 ₀₇ - 6 ₁₆	685	...	X	X
72.14	CH ⁺	$J = 5 - 4$	600	X
72.84	CO	$J = 36 - 35$	3700	...	X	...
78.74	o-H ₂ O	4 ₂₃ - 3 ₁₂	432	...	X	X
78.92	p-H ₂ O	6 ₁₅ - 5 ₂₄	396	...	X	...
79.11	OH	1/2 - 3/2 hfs	182	X	X	X
79.36	CO	$J = 33 - 32$	3092	X	X	...
89.99	p-H ₂ O	3 ₂₂ - 2 ₁₁	297	(Blend with CH ⁺)	X	...
90.02	CH ⁺	$J = 4 - 3$	297	X
90.16	CO	$J = 29 - 28$	2400	X	X	X
144.52	p-H ₂ O	4 ₁₃ - 3 ₂₂	396	...	X	...
144.78	CO	$J = 18 - 17$	945	X	X	X
145.52	[OI]	3P0-3P1	326	X	X	...
157.74	[CII]	2P3/2 - 2P1/2	91	X	X	...
158.31	p-H ₂ O	3 ₃₁ - 4 ₀₄	410
179.53	o-H ₂ O	2 ₁₂ - 1 ₀₁	115	(Blend with CH ⁺)	X	...
179.6	CH ⁺	$J = 2 - 1$	114	X
180.49	o-H ₂ O	2 ₂₁ - 2 ₁₂	194	...	X	...

An X indicates a detection.

TABLE 5

DETECTION STATISTICS OF PRIMARY ATOMIC AND MOLECULAR SPECIES

	[OI]63	[OI]145	[CII]157	H ₂ O 63	CO 18-17
Total	80/164	24/61	19/72	12/164	24/58
H AeBe stars ^a	20/25	5/23	6/25	2/25	10/24
T Tauri stars ^b	60/139	19/38	13/47	10/139	14/34

Each entry gives the number of targets detected and number observed. For [OI]145, [CII], and CO, observations were mostly carried out only if the lines were detected (or likely to be detected) in [OI]63 μm .

^aIncludes five young A stars classed as debris disks.

^bThis includes all stars observed which were not part of the HAeBe group.

2. A biased subset of the brighter objects from (1) were observed in [OI]145 μm , [CII]157 μm and CO $J = 18 - 17$, and the detection rates in this subset were 25–40% in each of these lines. Assuming that [OI]63 μm is always the easiest to detect (see above), then an unbiased sample of all 164 targets from (1) would have had a detection rate of $\sim 14\%$ in these other lines.

3. All HAeBe stars were detected in [OI]63 μm —a significantly higher detection rate than T Tauri systems. (Note that the statistics of HAeBe stars in Table 5 include five known A-star debris disks.)

4. The [OI]145 detection rate is a factor of ~ 2 higher in the T Tauri stars observed compared with HAeBe systems. This may reflect a higher [OI]63/145 μm line ratio in HAeBe disks.

5. The [CII] detection rate is similar (26%) in both T Tauri and HAeBe stars. If this is envelope material (see § 5.4), it indicates that compact envelopes of atomic gas can be maintained around both high and low-luminosity stars. Note, however, that in some cases the [CII] emission may be confused by ambient gas.

6. One (possibly two) HAeBe stars were detected in H₂O. Although in the small number regime, the H₂O detection rate is formally similar to that of T Tauri systems. However, considering the HAeBes are relatively bright in continuum compared with the T Tauri sample, this suggests that, on average, HAeBe systems are weaker in H₂O compared with T Tauri systems.

7. The fraction of objects with detectable warm CO (based on the $J = 18 - 17$ transition) is similar (40%) in disks around both types of stars.

5.3. [OI] Line Emission

As is clear from the example spectra, [OI]63 μm is normally several times brighter than any of the other FIR lines observed by GASPS, with an overall detection rate in the survey of $\sim 49\%$. In most cases, it is the best tracer (in the far-IR) of whether gas is present. This is true for almost all GASPS sources. To help understand the origin of the emission we can look at the data in more detail.

Most objects were unresolved in both line and continuum emission. An example is AA Tau (Fig. 6), where the ratio of flux in the centre to average of adjacent spaxels is ~ 20 . This

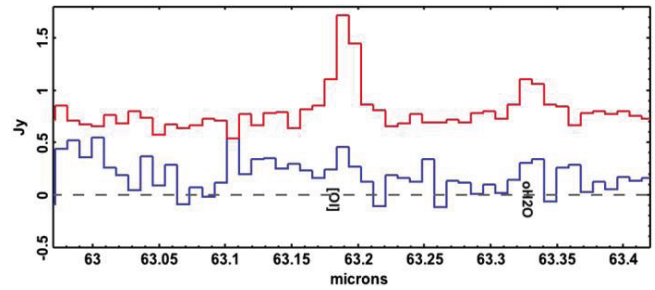


FIG. 6.—Spectra covering the [OI]63 μm line from the compact source AA Tau, in the central spaxel (*red histogram*), and an average of the eight adjacent spaxels (*in blue*). The adjacent pixel spectrum has been scaled up by a factor of 5 for clarity. Both the [OI]63 μm and nearby H₂O line are detected only in the central spaxel.

is consistent with an unresolved source, where we would expect the adjacent pixel average to be a few % of the centre, given an inter-spaxel spacing of 9.4", a PSF Gaussian equivalent width of $\sim 5.4''$ at 63 μm , the asymmetric sidelobes from PACS of a few percent, and taking into account possible pointing uncertainties of a few arcsec in some datasets (PACS User Manual, 2011). This lack of extended emission indicates a line emitting region of radius ≤ 500 AU.

For a number of individual unresolved objects with low accretion rates and no evidence of outflow we have assumed a disk origin and combined the [OI] fluxes with data at other wavelengths to estimate disk properties. Initial ProDiMo models of the relatively large disk in TW Hya (several 100 AU radius) indicate a gas mass of a few $10^{-3} M_{\odot}$ with gas-to-dust ratio a factor of ~ 10 lower than the ISM value (Thi et al. 2010), although some models suggest the gas mass an order of magnitude larger, with a more ISM-like gas-to-dust ratio (Gorti et al. 2011). ET Cha, by contrast, has a compact disk of modeled radius of only 10 AU, a low dust mass of a few $10^{-8} M_{\odot}$ and gas mass of a few $10^{-4} M_{\odot}$ (Woitke et al. 2011), suggesting either the gas-to-dust ratio is enhanced or there may be another contribution to the line flux. The HAeBe stars HD 169142 and HD 163296 both show emission consistent with disks and ISM-like values of the gas/dust ratio (Meeus et al. 2010; Tilling et al. 2012).

5.3.1. Spatially and Spectrally Resolved [OI]63 μm Emission: Outflow Jets

Although most objects in GASPS remain unresolved by PACS, five targets (identified in Appendix A) in Taurus were found to have clearly extended [OI]63 μm emission along known optical jets (Podio et al. 2012). Two of these also have broad line profiles in the centre. Figure 7 compares the spectrum of one example (RW Aur) with the unresolved line from AA Tau (*in red*), revealing a prominent red-shifted wing in RW Aur extending as much as $+200 \text{ km s}^{-1}$ from the stellar velocity. By

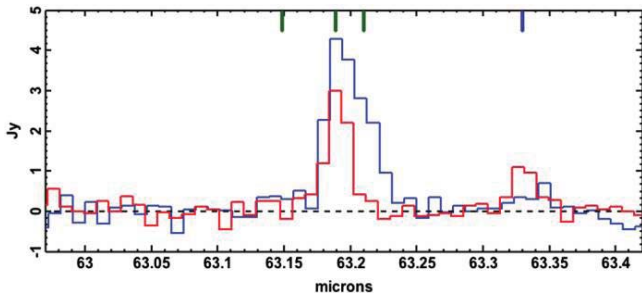


FIG. 7.—Spectrum of [OI]63 μm and H₂O from the jet source RW Aur (blue histogram), compared with AA Tau (red histogram), scaled up by a factor of 3 for easier comparison). These spectra are continuum-subtracted, and only the central spaxel is shown. AA Tau is unresolved whereas RW Aur has a prominent redshifted wing in [OI]. The velocities of the three components which dominate the [OI]6300 Å line are shown by the green tick marks, at the stellar velocity (heliocentric velocity +23 km s⁻¹) and at -190 and +100 km s⁻¹ (Hartigan et al. 1995). Also shown is the wavelength of the H₂O line, at the stellar velocity.

contrast, AA Tau has emission centred at the stellar velocity, with a fitted linewidth of 93 km s⁻¹ (FWHM)—similar to the measured PACS resolution of 88 km s⁻¹ at this wavelength (see PACS User Manual). The optical [OI]6300 Å line from RW Aur is known to originate from highly-excited gas in a jet of length a few arcsec (Melnikov et al. 2009), and the line-profile is dominated by three components (marked in Fig. 7), two at high velocities (+100 and -190 km s⁻¹), and one at the stellar velocity (Hartigan et al. 1995). The brighter red-shifted optical component corresponds with the [OI]63 μm wing, suggesting this is also from the shocked outflow gas (see § 4.2). However, the FIR line profile is dominated by emission centred approximately on the star, whereas this velocity component in the optical line is relatively weak (Hartigan et al. 1995). This low-velocity gas may be from the disk or disk wind (see above).

In the GASPS data we have also identified five other objects with evidence of either broadened lines or spatially-extended [OI]63 μm emission: HL Tau and XZ Tau (in the same PACS field), DO Tau, UZ Tau, and DK Cha (for the latter source, see van Kempen et al. [2010]). All targets resolved in [OI] are identified in Appendix A by the note ‘ext.OI’, and it is likely that [OI] emission is dominated by outflow gas in these cases.

5.3.2. Objects with Uncertain Origin of [OI]63 μm

In addition to the 10 resolved objects above, a further ~17 objects (noted as ‘jet’ sources in Appendix A) were identified as having published evidence of a high-velocity jet or outflow (Kenyon et al. 2008; Podio et al. 2012; Howard et al. 2013, in preparation). These are sources with a jet imaged in optical lines, a high velocity molecular outflow, or a broad (>50 km s⁻¹), typically blue-shifted, emission line profile in [O I] 6300 Å (see, e.g., Hartigan et al. [1995]). Three of these were HAeBe stars (HD 163296, MWC480, and HD 100546), leaving 14 T Tauri

‘jet’ sources. As noted in § 4.2, the survey sensitivity should allow us to detect [OI]63 μm emission from outflows shocks with mass loss rates $\dot{M} > 3 \times 10^{-9} M_{\odot}/\text{yr}$. Estimates from Hartigan et al. (1995) suggest that 4 of the jet sources in the Taurus sample have mass loss rates exceeding this limit (indicated in Appendix A by the note ‘high \dot{M} ’). However, their [OI]63 μm emission is neither spatially nor spectrally extended in the PACS data. This suggests that the outflow shock contribution may be small compared with the low-velocity gas; and, the origin of the unresolved [OI]63 μm emission in these remaining ‘jet’ sources is not clear from the PACS data alone.

5.4. [CII] Emission

The detection rate of [CII]157 μm in the survey was relatively low. For example, neither of the disks around AA Tau and HD 135344 were seen, yet both of these are among the most massive disks in the survey (total masses of $\sim 10^{-2} M_{\odot}$), with relatively rich spectra at other wavelengths. Woitke et al. (2010) predicted that the [CII] disk detection rate for Herschel/GASPS, assuming a wide range of grid parameters, should be 10–55%, and would be highly dependent on the UV excess (§ 4.1.2). Table 5 indicates a detection rate at the low end of this range: the brightest 44% of [OI]-detected objects were targeted for [CII] and of those, only ~26% were detected in [CII]. This might indicate that the low-UV models are more applicable to the sample. However, this is not supported by the [OI] detection rates, which are more consistent with moderate UV excesses (§ 5.5.1). Further investigation of this discrepancy is warranted.

A few objects showed extended [CII], or evidence of emission from the chop reference position, but in general problems from such confusion were limited (§ 2.1.4). There were, however, clear cases of both high- and low-mass objects with [CII]

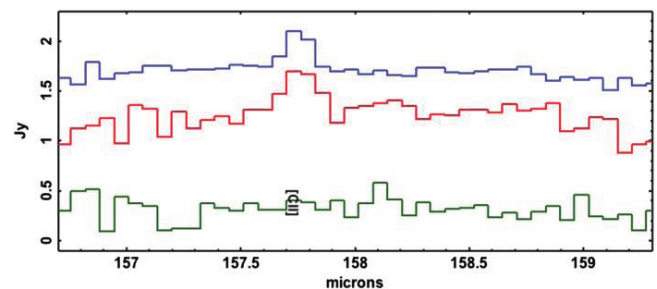


FIG. 8.—Spectra of [CII]157 from UY Aur in the central spaxel (blue histogram), and average of the 8 adjacent and 16 outer spaxels (red and green histograms, both scaled up by a factor of 6 for clarity). The emission in both line and continuum is centrally-peaked and consistent with the PSF response and the line-to-continuum ratio is similar in the central and first ring of spaxels, indicating that neither the line nor continuum are spatially extended compared with the beam.

emission centred on the star, examples being UY Aur and HD 100546. Figure 8 compares the spectra of UY Aur from the central spaxel with the middle ring of 8 and outer 16 spaxels in the PACS IFU. Both line and continuum are centrally peaked, with average fluxes consistent with the instrumental PSF size (11") at 157 μm . However, published coronagraph images shows that these objects also have scattered light extending over 5–10" (Hioki et al. 2007; Ardila et al. 2007) with a complex scattering morphology. This is larger than typical disk sizes and suggests emission may be from a compact envelope. The origin of [CII] line in these objects and whether it arises from the disk, compact envelope, or unresolved outflow is under investigation. But it suggests that the [CII] detection rate from the disks themselves might be even lower than indicated in Table 5.

5.5. Effect of System Parameters on Line Detectability

The GASPS target list (Appendix A) comprises a rich sample of Class II–III objects in the ~ 0.3 –30 Myr age range, and the survey detects [OI]63 μm from half of the targets observed. In the following, we investigate preliminary trends in line detectability vs. other directly-observed parameters. Results from GASPS papers on the individual associations (both published and in preparation) are combined to look at overall detection statistics. A minimum detection limit is 3σ and, although these were not all reduced with the same version of HIPE, the criteria for detection/non-detection is considered robust in this study. A more detailed investigation of correlations of line fluxes using systematically-calibrated data obtained from the same software version is left for a later paper.

5.5.1. Disk Dust Mass and [OI] Detections

The probability of [OI] detection in the GASPS survey is a strong function of the disk dust mass, M_d . This is illustrated in Figure 9, as a histogram of the detection rates as a function of distance-normalised dust mass, $M'_d = M_d \cdot (140/D)^2$, where D is the distance in pc. In this figure, we normalised the mass to an equivalent object giving the same flux at the distance of Taurus. We almost always detect the [OI]63 μm line when M'_d reaches a threshold of $\geq 10^{-5} M_\odot$: $84 \pm 10\%$ of targets were detected above this mass (where the uncertainty is the statistical error). This is comparable with the mass detection limit of sub-mm continuum surveys (e.g., Andrews & Williams [2005]), assuming a standard mass opacity, κ_ν . Assuming also an ISM-like gas/dust ratio can be used for all disks, this implies a total mass detection threshold for [OI]63 μm of $\sim 10^{-3} M_\odot$. If the gas-to-dust ratio is more typically $10\times$ lower (as has been suggested for TW Hya), then the [OI] observations are detecting disks with total masses $\geq 10^{-4} M_\odot$. As noted in § 5.3.1, some [OI]63 μm emission can be from outflows; on the plot we indicate in yellow the targets with spatially or spectrally-resolved [OI]. Additional targets (shown in green shading) are those with

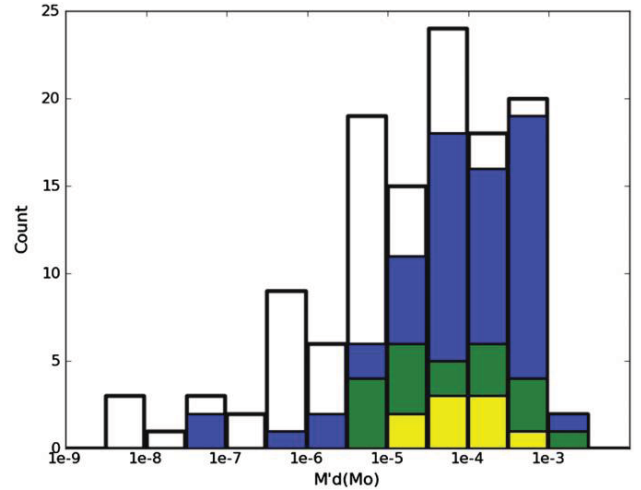


FIG. 9.—Distribution of normalised dust mass in the GASPS sample, illustrating the mass threshold for [OI]63 μm detection of a disk at the fiducial distance of 140 pc. Targets with [OI] detections are shown in shaded colours. The dust masses (in Solar units) are mostly based on published mm continuum observations, normalised to the distance of Taurus (140 pc), and assume a standard dust mass opacity (see text). Yellow shading indicates objects with extended energetic outflows, where the [OI] line is spatially or spectrally extended and includes some contribution from the jet (see § 5.3.1 and 5.3.2). Green shading indicates objects with evidence of an optical jet, but without spatially or spectrally-resolved [OI]63 μm emission; the contribution to the line from the jet in these objects is unclear.

published evidence of a high-velocity jet, although the contribution of this to the [OI]63 μm emission flux is unclear (see § 5.3.2).

The 84% detection rate for systems of $M'_d \geq 10^{-5} M_\odot$ drops to $32 \pm 12\%$ for $10^{-6} \leq M'_d \leq 10^{-5} M_\odot$. Woitke et al. (2010) constructed a large grid of disk models covering a parameter space similar to the that of the GASPS sample, and predicted overall [OI]63 μm detection rates of 51–70% for disks with dust masses of 10^{-7} – $10^{-3} M_\odot$ in systems with a high UV excess, and 17–30% for this mass range in the case of low UV. Restricting the model grid of Woitke et al. (2010) to include only disks of dust mass $> 10^{-5} M_\odot$, we find that such [OI] detection rates are achieved for moderate UV excesses ($0.01 \leq f_{\text{uv}} \leq 0.1$) and disk flaring ($1.0 < \beta < 1.2$). This suggests these ranges are typical of most systems in the survey.

There are some notable exceptions to the mass detection threshold, where we detected [OI] in systems with $M'_d < 3 \times 10^{-6} M_\odot$:

1. HD 172555, an unusual warm debris system with no evidence of molecular gas in mm lines, but with some indication that [OI] may be secondary gas released in collisions (Riviere-Marichalar et al. 2012b).
2. ET Cha, an apparently compact disk in the relatively old η Cha association (Woitke et al. 2011).

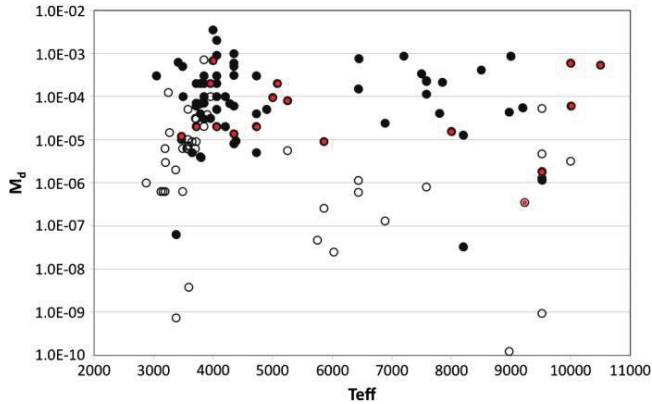


FIG. 10.—Disk dust mass of the GASPS sample, normalised to a distance of 140 pc (*units of M_{\odot}*), plotted as a function of the stellar effective temperature (*in K*). This illustrates the line detectability of a disk of a given dust mass at the distance of the Taurus star forming region. [OI]63 μm detections are shown as *filled circles*, and *open circles* depict [OI] upper limits. An additional *red dot* indicates systems which were detected in [CII].

3. J130521.6-773810, although the classification of this target in ChaII is uncertain.

4. 51 Oph, a warm compact disk with notable hot and compact molecular gas component (Thi et al., submitted).

5. HD141569, a diffuse disk with spiral structure around a HAeBe star (Clampin et al. 2003).

The number of disks with published dust masses as low as $10^{-8} M_{\odot}$ is relatively small (only ~ 10 in GASPS have measured values), and further mm-wavelength measurements of such disks would be interesting to improve the statistics. At the opposite extreme, three relatively massive disks ($M'_d \geq 10^{-4} M_{\odot}$) have no evidence of [OI]63 μm : GO Tau, V836 Tau, and TWA03. Woitke et al. (2010) indicate that disks of this

mass which have low flaring ($\beta \leq 1.0$) can have [OI]63 μm fluxes too low to be detected by GASPS.

5.5.2. Dependence on Spectral Type

It is already clear from Table 5 that [OI]63 μm is significantly easier to detect around HAeBe stars than T Tauri stars. Is this simply because HAeBe disks in the sample are more massive and the detection threshold is more commonly reached? Figure 10 shows the distribution of normalised disk dust masses (M'_d) in GASPS as a function of stellar T_{eff} . Systems detected in [OI] and [CII] are indicated by the filled black and red symbols respectively. This shows that both early and late-type stars have a similar range of disk dust masses in this sample. As noted above, the [OI] detection rate is high for disks with $M'_d > 10^{-5} M_{\odot}$, and Figure 10 shows that this is independent of T_{eff} for $T_{\text{eff}} > 4000$ K. However, approximately half of the low-luminosity stars ($T_{\text{eff}} < 4000$ K, or M type) with M'_d in the range 10^{-5} to $10^{-4} M_{\odot}$ were not detected. Clearly the spectral type has some effect on the [OI] line emission threshold for the lowest-luminosity stars.

In the case of the [CII]157 line, the detectability in Figure 10 seems to be independent of the spectral type and disk mass, with [CII] detections (*filled red symbols*) broadly distributed over the M'_d - T_{eff} parameter space. Unlike [OI], there is no clear threshold with disk mass, or an increase in detection rate among HAeBe stars. If most [CII] arises from a compact envelope rather than the disk, this suggests that such gas may be retained around these stars independent of the mass of the inner disk or stellar type.

5.5.3. Other Observational Parameters: Binarity, $H\alpha$, and X-ray Luminosity

The histograms in Figures 11 and 12 show the detection statistics for targets searched in [OI]63 μm with published X-ray

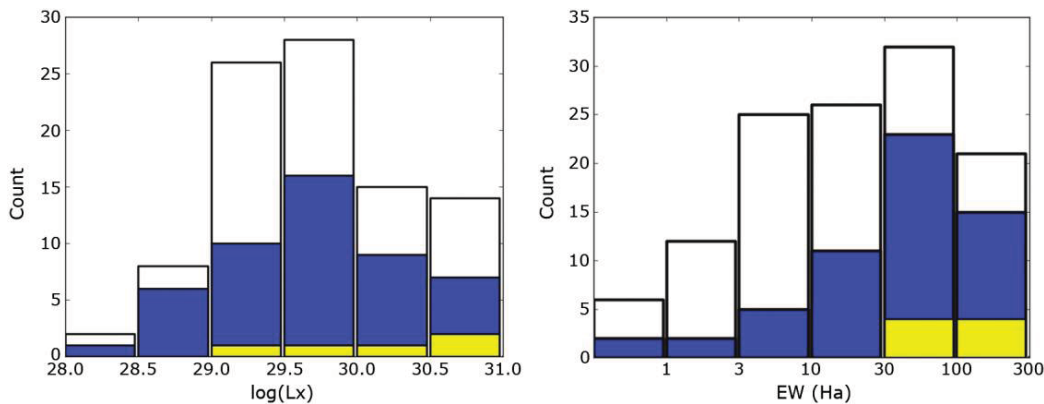


FIG. 11.—Histogram of the distribution of (a) X-ray luminosity (erg s^{-1}) and (b) $H\alpha$ EW (\AA) of the GASPS sample observed in [OI]63 μm . The [OI] detections are shaded in *blue*, with the *yellow* shading indicating those with an extended [OI] component. There is no clear dependence of [OI] detectability on X-ray luminosity, but detection rates are higher for larger $H\alpha$ EW.

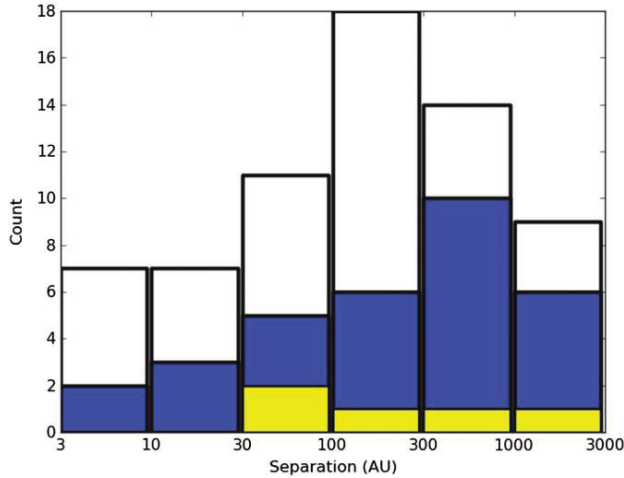


FIG. 12.—Histogram of the distribution of binary separation (in AU) in the sample observed in [OI]63 μm , with line detections shaded in blue. Binary stars with known extended jet contribution to the [OI]63 μm flux are shaded further in yellow.

luminosity, $H\alpha$ equivalent width (EW) and binary separation. The numbers of targets with [OI] detections are shaded. Those which have additional extended [OI]63 μm emission from a jet are shaded yellow. Figure 11a shows that line emission is detected in systems covering the full range of X-ray luminosity in the survey, with no clear trend of increased detectability for higher X-ray fluxes. The $H\alpha$ EW used in Figure 11b is linked with the accretion rate, although later-type K stars may have significant chromospheric contribution and the accretion luminosity may be lower than Figure 11b might suggest. But there is a trend of increasing [OI] detection probability for higher accretion rates, including all stars observed. The detection fraction is 70% for EW >30 Å (or 67% excluding the stars with extended jet emission) compared with only 29% for those with lower EW. A systematic derivation of accretion luminosity and line flux

over the whole survey would be interesting to study further correlations between the [OI]63 μm flux and accretion rates.

Figure 12 illustrates the [OI] detection rates distributed over binary separation. For hierarchical multiples we have used the separation of the widest component within the PACS beam. There is marginal evidence for a drop in detection rates in multiples of separation <300 AU, from 64% for the wider binaries to 40% for the closer systems (with statistical errors of $\sim 10\%$). By comparison, the [OI] detection fraction of single stars in the sample was 47%. This would suggest that most [OI] emission arises from radii of <300 AU—similar to the [OI]-emitting region suggested by the models in Figure 1. By comparison, samples of T Tauri stars observed in mm dust indicate that M_d typically drops by a factor of 5 for binary separations of <300 AU (Harris et al. 2012).

5.5.4. Detection Rates in Different Associations and Dependence on Age

In Table 6 we give the [OI]63 μm detection rates for the different associations observed in GASPS, for those with and without published dust masses (for masses based on continuum photometry, although only two disks were detected which had no published estimates). As noted above, the required dust mass (M'_d) for [OI]63 μm to be detected at a distance of 140 pc is $\sim 10^{-5} M_\odot$, or a total (gas+dust) mass of $1 M_{\text{Jupiter}}$, assuming an ISM gas-to-dust ratio. The detection rates are somewhat dependent on spectral type (M stars have a higher disk mass threshold for detection—see Fig. 10), binarity (lower for separations <300 AU), and accretion rates (more for $H_\alpha > 30$ Å). However, if we use [OI]63 μm detections as a proxy for $1 M_{\text{Jupiter}}$ disks at the fiducial 140 pc distance, it is possible to compare the detection rates in different associations, modulo the distances, and assume we are sampling most of the brighter detectable disks. Each of the three intermediate-age (5–10 Myr) associations (η Cha, TWA and upper Sco) has ~ 2 –3 such disks. TWA is significantly closer, and only one of these would be

TABLE 6
DETECTION STATISTICS OF [OI]63 μm FOR THE ASSOCIATIONS IN GASPS, WITH AND WITHOUT KNOWN DISK MASSES

Association	M_d		No M_d^a		Total	
	Detected	Observed	Detected	Observed	Detected	Observed
Taurus	44	56	1	17	45	73
Cha II	7	17	1	2	8	19
η Cha	2	7	0	6	2	13
TW Hya	3	5	0	3	3	8
Upper Sco	2	7	0	12	2	19
β Pic	1	4	0	1	2 ^b	6
Tuc Hor	0	2	0	0	0	2
H AeBe stars	20	25 ^c	0	0	20	20

^a No disk masses were available from the literature.

^b Includes detection of β Pic itself (Brandeker et al. [2011]).

^c Five nondetected systems are those classed as possible debris disks.

detected by GASPS if moved to the fiducial distance of 140 pc. The *total* number of stars in the upper Sco group is ~ 200 (Carpenter et al. 2009), with 20–50 in the two other associations in this age range (Torres et al. 2008), giving a gas-detected disk fraction of 1–7% at 5–10 Myr. For the older systems, there are two unusual [OI]-emitting disks in the 10–20 Myr β Pic moving group but neither would have been detected at 140 pc, and no disks were detected in [OI] in the 30-Myr old Tuc Hor association. Each of these contains ~ 40 stars (Torres et al. 2008). For the two younger groups, the detection rate in GASPS was $\sim 50\%$. However, the total number of stars is estimated to be ~ 250 in Taurus and ~ 48 in Cha II (Rebull et al. 2010; Alcalá et al. 2008), giving massive disk fractions of ~ 18 and 17%, respectively. For the HAeBe stars in the sample (excluding debris disks), the derived ages are mostly in the range 2–10 Myr (Montesinos et al. 2009; Meeus et al. 2012), and the [OI] fraction is $\sim 100\%$, much higher than the equivalent-aged FGKM star. While not a statistically-complete sample of AeBe stars in this age range, it suggests either that these more luminous stars are more commonly able to retain disks, or that their ages are overestimated. Overall, for T Tauri stars, the fraction with Jupiter-mass, gas-rich disks is $\sim 18\%$ at ages of 0.3–4 Myr, 1–7% at 5–10 Myr, and none are detected beyond 10 Myr age. It is unclear why some particular stars can retain these gas-rich disks for up to 10 Myr, and whether planets formed in such long-lived disks would be different from those around other stars.

6. CONCLUSIONS

In this article we describe the GASPS far-infrared survey of gas and dust in young stellar systems. This Herschel Key project observed selected lines and continuum with the PACS instrument, targetting 250 young SED-Class II–III systems, Herbig AeBe stars, and young debris disks. The far-IR line emission can arise from the hot surface of gas disks around 30–300 AU, high-velocity jet shocks, disk winds and/or compact remnant envelopes. We outline the models used to predict disk line strengths and their dependence on disk parameters, and look at the possible emission from these other mechanisms, in particular from extended outflow jets in a few objects. The master list of targets with basic system parameters is presented, and we also indicate in this list which objects have detections in the primary GASPS lines.

The FIR lines are identified and we show preliminary line detection statistics, referring to the published papers which analyse individual sources and associations in more detail. Rich

spectra were seen in a number of sources, including fine-structure atomic lines of [OI] at 63 and $145\mu\text{m}$, and [CII] at $157\mu\text{m}$, as well as molecules including high-J transitions of CO, H_2O , OH and CH^+ . In most systems, [OI]63 μm was the brightest line by a factor of ~ 10 , and is associated in most cases with disk emission. Line and continuum emission was, in all but 10 systems, both spatially and spectrally unresolved and centred on the star. For the extended sources, emission is thought to arise from jet shocks, along with a disk contribution. The [CII]157 line was significantly weaker than [OI], resulting in a relatively low detection rate. However, in a small number of objects unresolved emission was found centred on the star, and may arise from a compact remnant envelope.

49% of all targets observed were detected in [OI]63 μm , with an 84% detection rate for those having disk dust masses of $\geq 10^{-5} M_\odot$. Comparison with statistics from a grid of model implies that most systems have moderate UV excesses and disk flaring. Assuming an ISM gas-to-dust ratio of 100 and typical mm-wavelength mass opacity, this represents an [OI] detection threshold for the *total* disk mass of $\sim 1 M_{\text{Jupiter}}$. Going against this trend, we find five unusually low disk mass systems with [OI]63 μm emission, and a few high-mass systems which remained undetected. The [OI]63 μm detection rates were independent of X-ray luminosity, but there was evidence of a decreased rate in binaries of separation < 300 AU, in stars with $\text{H}\alpha$ EW < 30 Å, and for M-type stars. Based on [OI]63 μm line detections, the results show that $\sim 18\%$ of stars in each association can retain gas-rich disks of minimum mass $10^{-3} M_\odot$ for up to 4 Myr, a few % of stars keep these disks for ~ 5 –10 Myr, but none are detected beyond 10–20 Myr.

We wish to acknowledge the Herschel Helpdesk for their timely and useful responses. The Grenoble group thanks ANR (contracts BLAN-0221, 0504-01 and 0505-01), European Commission's 7th Framework program (contract pERG06-GA-2009-256513), CNES, and PNPS of CNRS/INSU, France for support. PW, IK, and WFT acknowledge funding from the EU FP7-2011 under Grant Agreement nr. 284405. WFT acknowledges a Scottish University physics Alliance fellowship (2006-2009). PACS has been developed by a consortium of institutes led by MPE (Germany) and including UVIE (Austria); KU Leuven, CSL, IMEC (Belgium); CEA, LAM (France); MPIA (Germany); INAF-IFSI/OAA/OAP/OAT, LENS, SISSA (Italy); IAC (Spain). This development has been supported by the funding agencies BMVIT (Austria), ESA-PRODEX (Belgium), CEA/CNES (France), DLR (Germany), ASI/INAF (Italy), and CICYT/MCYT (Spain).

APPENDIX A

TARGET LIST

TABLE A1
INITIAL TARGET LIST

ID	Name	RA	DEC	Dist.	Sp.T. ^a	Sep. ^b	log(L_p) ^c	$W_{\text{H}\alpha}$ ^d	SED ^e	M_{dust}^f	OI/ClI/ CO/H ₂ O ^g	Notes/refs. ^h
T-1	HBC 347	03 29 38.37	+24 30 38.0	140	K1	0.2	III	<4.0e-6	0/1/0	
T-2	HBC 351	03 52 02.24	+24 39 47.9	140	K5	0.61	...	2.8	III	<5.0e-6	:/:/:	i
T-3	HBC 352/353	03 54 29.51	+32 03 01.4	140	G0	8.6	30.4	<	III	<5.0e-6	:/:/:	i
T-4	HBC 354/355	03 54 35.56	+25 37 11.1	140	K3	6.3	...	<	III	<4.0e-6	:/:/:	i
T-5	SAO 76411	04 02 53.57	+22 08 11.8	140	G1	1	III	<5.0e-6	:/:/:	
T-6	HBC 356/357	04 03 13.96	+25 52 59.8	140	K2	2.0	...	1	III	<4.0e-6	0/1/0	i
T-7	HBC 358/359	04 03 50.84	+26 10 53.2	140	M2	1.6	29.8	7	III	<5.0e-6	0/1/0	
T-8	SAO 76428	04 04 28.49	+21 56 04.6	140	F8	1.3	III	<6.0e-6	:/:/:	
T-9	HBC 360/361	04 04 39.37	+21 58 18.6	140	M3	7.2	...	6.6	III	<7.0e-6	:/:/:	
T-10	HBC 362	04 05 30.88	+21 51 10.7	140	M2	6.6	III	<4.0e-6	:/:/:	
T-11	LkCa 1	04 13 14.14	+28 19 10.8	140	M4	...	29.3	3.5	III	<4.0e-6	0:0	
T-12	Anon 1	04 13 27.23	+28 16 24.8	140	M0	0.015	30.5	2.5	III	<4.0e-6	0/1/0	
T-13	V773 Tau A-D	04 14 12.92	+28 12 12.4	140	K2	0.2	30.9	3.0	II	5.0e-6	1/1/0	Jet. Hierarchical 37'' from V773Tau
T-14	FM Tau	04 14 13.58	+28 12 49.2	140	M0	...	29.7	76	II	2.0e-5	0/0/0/0	Jet, High M
T-15	CW Tau	04 14 17.0	+28 10 57.8	140	K3	...	30.4	140	II	2.0e-5	1/1/1/0	
T-16	CX Tau	04 14 47.86	+26 48 11.0	140	M3	18	II	1.0e-5	1/1/0	
T-17	LkCa 3 AB	04 14 47.97	+27 52 34.6	140	M1	0.47	29.8	2.7	III	<4.0e-6	0/1/0	
T-18	FO Tau AB	04 14 49.29	+28 12 30.6	140	M2	0.15	28.7	126	II	6.0e-6	0/0/0/0	
T-19	CIDA-2	04 15 05.16	+28 08 46.2	140	M5.5	...	29.1	6	III	<7.0e-6	0/1/0	
T-20	LkCa 4	04 16 28.11	+28 07 35.8	140	K7	...	30.0	3.2	III	<2.0e-6	0/1/0	
T-21	CY Tau	04 17 33.73	+28 20 46.8	140	M1.5	...	29.3	63	II	6.0e-5	1/1/0	
T-22	LkCa 5	04 17 38.94	+28 33 00.5	140	M2	0.048	29.7	3.8	III	<2.0e-6	0/1/0	
T-23	HBC 372	04 18 21.47	+16 58 47.0	140	K5	<	III	<4.0e-6	:/:/:	
T-24	HBC 376	04 18 51.70	+17 23 16.6	140	K7	1.9	III	<3.0e-6	:/:/:	
T-25	04158+2805	04 18 58.14	+28 12 23.5	140	M3	175	I-II	3.0e-4	1/0/1/0	Jet
T-26	FQ Tau AB	04 19 12.81	+28 29 33.1	140	M3	0.76	28.8	97	II	1.0e-5	0/0/0/0	
T-27	BP Tau	04 19 15.84	+29 06 26.9	140	K7	...	30.2	66	II	2.0e-4	1/1/0	
T-28	V819 Tau AB	04 19 26.26	+28 26 14.3	140	K7	10.5	30.3	2.5	III	<4.0e-6	0/0/1/0	
T-29	LkCa 7 AB	04 19 41.27	+27 49 48.5	140	K7	1.04	29.9	3.9	III	<4.0e-6	0/1/0	
T-30	DE Tau	04 21 55.64	+27 55 06.1	140	M2	59	III	5.0e-5	0/0/1/0	
T-31	RY Tau	04 21 57.40	+28 26 35.5	140	K1	...	30.7	13	II	2.0e-4	1/1/0/1	Jet
T-32	HD 283572	04 21 58.85	+28 18 06.6	140	G5	...	31.1	<	III	<4.0e-6	0/1/0	
T-33	T Tau NS	04 21 59.43	+19 32 06.4	140	K0	0.7	30.9	40	I-II	8.0e-5	1/1/1/1	Ext.OI, Po12
T-34	FS Tau AB	04 22 02.18	+26 57 30.5	140	M0	0.25	30.9	69	II	2.0e-5	1/1/1/1	Ext.OI, Po12
T-35	LkCa 21	04 22 03.14	+28 25 39.0	140	M3	0.044	30.9	6.1	III	<5.0e-6	:/:/:	
T-36	FT Tau	04 23 39.19	+24 56 14.1	140	M3	254	II	1.0e-4	1/1/0	
T-37	IP Tau	04 24 57.08	+27 11 56.5	140	M0	10.5	II	3.0e-5	1/1/0	
T-38	J1-4872 AB	04 25 17.68	+26 17 50.4	140	K7	3.3	29.7	2.9	III	<4.0e-6	0/1/0	
T-39	DG Tau B	04 27 02.56	+26 05 30.7	140	< K6	...	31.0	270	I-II	6.8e-4	1/1/1/0	Ext.OI, Po12
T-40	DF Tau AB	04 27 02.80	+25 42 22.3	140	M0.5	0.07	29.1	54.5	II	4.0e-6	1/0/0/0	Jet, high M

TABLE A1 (Continued)

ID	Name	RA	DEC	Dist.	Sp.T. ^a	Sep. ^b	log(L_{FIR}^c)	$W_{\text{H}\alpha}^d$	SED ^e	M_{dust}^f	OI/CII/ CO/H ₂ O ^g	Notes/refs. ^h
T-41	DG Tau A	04 27 04.70	+26 06 16.3	140	K6	...	29.4	90	I-II	2.0e-4	1/1/1/0	Ext.OI, high M , Po12
T-42	HBC 388	04 27 10.57	+17 50 42.6	140	K1	<	III	<3.0e-6	:/:/:/	
T-43	J1-507	04 29 20.71	+26 33 40.7	140	M4	0.08	29.6	5.1	III	<3.0e-6	:/:/:/	
T-44	FW Tau ABC	04 29 29.71	+26 16 53.2	140	M4	0.2	...	17	III	2.0e-6	0/:/0	Jet, Mult.
T-45	DH/DI Tau	04 29 42.02	+26 32 53.2	140	M2/M2	2.3	30.9	35/2	II/III	3.0e-5	0/:/0	
T-46	IQ Tau	04 29 51.56	+26 06 44.9	140	M0.5	...	29.5	12	II	2.0e-4	1/0/0/0	
T-47	UX Tau B/AC	04 30 04.00	+18 13 49.4	140	K1	2.7	29.9	4	II/III	5.0e-5	1/:/0	Mult.
T-48	FX Tau AB	04 30 29.61	+24 26 45.0	140	M1	0.9	29.6	12	II	9.0e-6	0/:/0	
T-49	DK Tau AB	04 30 44.25	+26 01 24.5	140	K7	2.3	30.0	40	II	5.0e-5	1/0/0	
T-50	ZZ Tau	04 30 51.38	+24 42 22.3	140	M3	0.04	...	14	III	<4.0e-6	0/:/0	
T-51	JH 56	04 31 14.44	+27 10 18.0	140	M0.5	2.2	III	<4.0e-6	:/:/:/	
T-52	V927 Tau AB	04 31 23.82	+24 10 52.9	140	M5.5	0.29	29.2	10	III	<5.0e-6	0/:/0	
T-53	HBC 392	04 31 27.17	+17 06 24.9	140	K5	1.1	III	<3.0e-6	:/:/:/	
T-54	XZ Tau AB	04 31 40.07	+18 13 57.2	140	M1.5	0.3	29.9	274	II	1.2e-5	1/1/1/1	Jet, ext.OI, +HL Tau
T-55	HK Tau AB	04 31 50.57	+24 24 18.1	140	M0.5	2.4	28.9	42	I-II	4.0e-5	1/0/1/0	
T-56	V710 Tau AB	04 31 57.79	+18 21 38.1	140	M0.5	3.1	30.1	61	II	7.0e-5	1/:/0	
T-57	J1-665	04 31 58.44	+25 43 29.9	140	M5	...	28.8	5.2	III	<4.0e-6	:/:/:/	
T-58	L1551-51	04 32 09.27	+17 57 22.8	140	K7	...	30.2	1.5	III	<6.0e-6	:/:/:/	
T-59	V827 Tau	04 32 14.57	+18 20 14.7	140	K7	0.09	30.6	3	III	<3.0e-6	1/:/0	
T-60	Haro 6-13	04 32 15.41	+24 28 59.7	140	M0	...	29.2	61	I-II	1.0e-4	1/0/1/0	Jet
T-61	V826 Tau AB	04 32 15.84	+18 01 38.7	140	K7	0.014	30.6	3	III	<4.0e-6	:/:/:/	
T-62	V928 Tau AB	04 32 18.86	+24 22 27.2	140	M0.5	0.2	30.0	1.5	III	<4.0e-6	:/:/:/	
T-63	GG Tau AB	04 32 30.35	+17 31 40.6	140	K7	0.25	28.6	50	II	2.0e-3	1/0/0/0	Mult.
T-64	UZ Tau EW	04 32 43.04	+25 52 31.1	140	M1	3.5	29.9	73	II	2.0e-4	1/0/0/0	Jet, ext.OI, high M , Mult.
T-65	L1551-55	04 32 43.73	+18 02 56.3	140	K7	...	29.8	1.0	III	<3.0e-6	:/:/:/	
T-66	GH/V807 Tau	04 33 06.43	+24 09 44.5	140	M2/K7	0.3	29.1/30.0	20/10	II/III	7.0e-6	0/0/0	Mult.
T-67	V830 Tau	04 33 10.03	+24 33 43.4	140	K7	...	30.7	2.5	III	<3.0e-6	:/:/:/	
T-68	GI/GK Tau	04 33 34.31	+24 21 11.4	140	K6/K7	13	29.9/30.1	18/25	II/III	2.0e-5	1/:/1	Jet, GK is binary
T-69	DL Tau	04 33 39.06	+25 20 38.2	140	K7	101	II	9.0e-4	1/0/1	Jet, high M
T-70	HN Tau AB	04 33 39.35	+17 51 52.4	140	K5	3.1	29.2	145	II	8.0e-6	1/0/0/0	
T-71	DM Tau	04 33 48.72	+18 10 10.0	140	M1	...	29.3	114	II	2.0e-4	1/0/0	
T-72	CI Tau	04 33 52.00	+22 50 30.2	140	K7	...	29.5	90	II	3.0e-4	1/0/0/0	
T-73	J2-2041	04 33 55.47	+18 38 39.1	140	M3.5	0.42	...	4.7	:/:/:/	
T-74	JH 108	04 34 10.99	+22 51 44.5	140	M1	...	30.0	3	III	<4.0e-6	:/:/:/	
T-75	HBC 407	04 34 18.04	+18 30 06.6	140	G8	0.14	...	<	III	<4.0e-6	:/:/:/	
T-76	Wa Tau/I	04 34 39.29	+25 01 01.0	140	K0	0.5	III	<3.0e-6	:/:/:/	
T-77	AA Tau	04 34 55.42	+24 28 53.2	140	K7	...	30.0	42	II	1.0e-4	1/0/1	
T-78	HO Tau AB	04 35 20.20	+22 32 14.6	140	M0.5	6.9	29.5	108	II	2.0e-5	0/:/0	
T-79	FF Tau AB	04 35 20.90	+22 54 24.2	140	K7	0.03	29.8	2	III	<2.0e-6	0/:/0	

TABLE A1 (Continued)

ID	Name	RA	DEC	Dist.	Sp. T. ^a	Sep. ^b	log(L_p) ^c	$W_{\text{H}\alpha}$ ^d	SED ^e	M_{dust}^f	OI/CH/ CO/H ₂ O ^g	Notes/refs. ^h
T-80	HBC 412 AB	04 35 24.51	+17 51 43.0	140	M2	0.7	...	9	III	<4.0e-6	:/:/:	
T-81	DN Tau	04 35 27.37	+24 14 58.9	140	M0	...	30.0	45	II	3.0e-4	1/0:/0	
T-82	LkCa 14	04 36 19.09	+25 42 59.0	140	M0	1.1	III	<4.0e-6	:/:/:	
T-83	HD 283759	04 36 49.12	+24 12 58.8	140	F2	III	<4.0e-6	:/:/:	
T-84	DO Tau	04 38 28.58	+26 10 49.4	140	M0	101	II	7.0e-5	1/0/1/0	Ext.OI, jet, high \dot{M}
T-85	HV TauABC	04 38 35.28	+26 10 38.6	140	M1/M4	4.0	29.57	10	III/II	2.0e-5	1:/:/0	Jet, Mult.
T-86	VY Tau AB	04 39 17.41	+22 47 53.4	140	M0	0.66	...	7.3	II	<5.0e-6	0:/:/0	
T-87	LkCa 15	04 39 17.80	+22 21 03.5	140	K5	18.5	II	5.0e-4	1/0/0/0	
T-88	JH 223	04 40 49.51	+25 51 19.2	140	M2	2.1	28.8	4	II	<3.0e-6	:/:/:	
T-89	IW TauAB	04 41 04.71	+24 51 06.2	140	K7	0.28	30.0	4	III	<4.0e-6	:/:/:	Jet
T-90	CoKuTau/4	04 41 16.81	+28 40 00.1	140	M1.5	0.05	...	3	II	5.0e-6	1:/:/0	
T-91	04385+2550 (Har06-33)	04 41 38.8	+25 56 26.8	140	M0	19	29.6	17	I-II	...	1:/:/0	
T-92	DP Tau	04 42 37.70	+25 15 37.5	140	M0.5	0.11	29.0	87	II	<5.0e-6	1/1/1/0	Jet
T-93	GO Tau	04 43 03.10	+25 20 18.7	140	M0	...	29.4	80	II	7.0e-4	0:/:/0	
T-94	DQ Tau AB	04 46 53.04	+17 00 00.5	140	K5	0.0004	...	102	II	2.0e-4	1/0:/0	
T-95	Har0 6-37 AB	04 46 58.98	+17 02 38.2	140	K7	2.6/0.3	...	13	II	1.0e-4	1:/:/0	
T-96	DS Tau	04 47 48.11	+29 25 14.4	140	K5	7.1	...	38	II	6.0e-5	1:/:/0	
T-97	UY Aur AB	04 51 47.37	+30 47 13.5	140	K7	0.88	...	63	II	2.0e-5	1/1/1/1	Jet, high \dot{M}
T-98	St 34	04 54 23.68	+17 09 53.5	110	M3	1.2	...	90	II	<5.0e-6	:/:/:	
T-99	GM Aur	04 55 10.99	+30 21 59.2	140	K3	...	29.8	79	II	3.0e-4	1/0/0/0	
T-100	LkCa 19	04 55 36.96	+30 17 55.3	140	K0	...	30.7	1.2	III	5.0e-6	:/:/:	
T-101	AB Aur	04 55 45.83	+30 33 04.4	140	A0	...	29.5	33	II	4.0e-5	1/1/1/0	
T-102	SU Aur	04 55 59.38	+30 34 01.6	140	G2	...	31.1	4	II	9.0e-6	1/1/1/0	Jet
T-103	HBC 427	04 56 02.02	+30 21 03.7	140	K7	0.03	30.5	1.4	III	<7.0e-6	:/:/:	
T-104	V836 Tau	05 03 06.60	+25 23 19.7	140	K8.5	...	30.0	7.7	II	1.0e-4	0:/:/0	
T-105	CIDA-10	05 06 16.75	+24 46 10.2	140	M4	0.08	29.0	9	III	<5.0e-6	:/:/:	
T-106	RW Aur AB	05 07 49.54	+30 24 05.1	140	K1	1.4	...	75	II	4.0e-5	1/0/1/0	Ext.OI, Po12
S-1	HIP 76310	15 35 16.10	-25 44 03.1	150	A0V	<	D	3.6e-6	0:/:/0	
S-2	J153557.8-232405	15 35 57.80	-23 24 04.6	145	K3	0.05	30.04	<	III	<4.2e-6	:/:/:	
S-3	J154413.4-252258	15 44 13.34	-25 22 59.1	145	M1	...	30.0	3.2	III	<4.2e-6	:/:/:	
S-4	HIP 77815	15 53 21.93	-21 58 16.5	171	A5V	—	<3.0e-6	:/:/:	
S-5	HIP 77911	15 54 41.60	-22 45 58.5	147	B9V	7.96	...	<	D	<3.5e-6	0:/:/0	
S-6	J155624.8-222555	15 56 24.77	-22 25 55.3	145	M4	5.4	II	<3.7e-6	:/:/:	
S-7	HIP 78099	15 56 47.85	-23 11 02.6	140	A0V	<	...	<4.2e-6	:/:/:	
S-8	J155706.4-220606	15 57 06.42	-22 06 06.1	145	M4	3.6	II	<4.3e-6	:/:/:	
S-9	J155729.9-225843	15 57 29.86	-22 58 43.8	145	M4	7.0	II	<3.7e-6	0:/:/0	
S-10	J155829.8-231007	15 58 29.81	-23 10 07.7	145	M3	250	II	<3.4e-6	0:/:/0	
S-11	RXJ1600.7-2343	16 00 44.60	-23 43 12.0	145	M2	1.46	30.4	...	III	<3.8e-6	0:/:/0	
S-12	J160108.0-211318	16 01 08.01	-21 13 18.5	145	M0	...	30.3	2.4	III	<4.0e-6	:/:/:	
S-13	J160210.9-200749	16 02 10.96	-20 07 49.6	145	M5	3.5	III	<3.7e-6	:/:/:	
S-14	J160245.4-193037	16 02 45.45	-19 30 37.8	145	M5	28.2	...	1.1	III	<3.6e-6	:/:/:	

TABLE A1 (Continued)

ID	Name	RA	DEC	Dist.	Sp.T. ^a	Sep. ^b	log(L_{FIR}^c)	$W_{\text{H}\alpha}^d$	SED ^e	M_{dust}^f	OI/CII/ CO/H ₂ O ^g	Notes/refs. ^h
S-15	J160357.6-203105	16 03 57.68	-20 31 05.5	145	K5	12	II	<3.7e-6	0/0/0/0	
S-16	J160357.9-194210	16 03 57.94	-19 42 10.8	145	M2	3.0	II	<3.7e-6	0/0/0	
S-17	J160421.7-213028	16 04 21.66	-21 30 28.4	145	K2	16.22	30.3	0.6	II-III	1.1e-4	1/1/0/0	
S-18	J160525.5-203539	16 05 25.56	-20 35 39.7	145	M5	6.1	III	<5.4e-6	:/:/:	
S-19	J160532.1-193315	16 05 32.15	-19 33 16.0	145	M5	2.6	III	<3.9e-6	0/0/0	
S-20	J160545.4-202308	16 05 45.40	-20 23 08.8	145	M2	3.5	II	7.7e-6	0/0/0/0	
S-21	J160600.6-195711	16 06 00.62	-19 57 11.5	145	M5	7.5	II	<4.9e-6	0/0/0	
S-22	ScoPMS 31	16 06 21.96	-19 28 44.6	145	M0.5V	0.58	30.1	2.1	II	4.1e-6	0/0/0	
S-23	J160622.8-201124	16 06 22.78	-20 11 24.4	145	M5	6.0	II	<4.3e-6	:/:/:	
S-24	J160643.8-190805	16 06 43.86	-19 08 05.6	145	K6	2.4	:/:/:	
S-25	J160654.4-241610	16 06 54.36	-24 16 10.8	145	M3	1.50	29.9	3.6	:/:/:	
S-26	J160702.1-201938	16 07 02.12	-20 19 38.8	145	M5	1.63	...	3.0	II	<3.7e-6	:/:/:	
S-27	HIP 78996	16 07 29.93	-23 57 02.3	108	A9V	<	D	<4.2e-6	:/:/:	
S-28	J160801.4-202741	16 08 01.42	-20 27 41.7	145	K8	...	29.9	2.3	:/:/:	
S-29	J160823.2-193001	16 08 23.25	-19 30 00.9	145	K9	6.0	II	4.4e-5	0/0/0/0	
S-30	J160827.5-194904	16 08 27.52	-19 49 04.7	145	M5	12	III	<5.3e-6	:/:/:	
S-31	J160856.7-203346	16 08 56.73	-20 33 46.0	145	K5	...	30.1	0.5	:/:/:	
S-32	J160900.7-190852	16 09 00.39	-19 08 44.8	145	K9	...	30.0	1.3	II	2.5e-5	:/:/:	With J160900.0- 190836
S-33	HIP 79156	16 09 20.89	-19 27 25.9	170	A0V	0.89	...	<	D	<3.3e-6	:/:/:	
S-34	J160953.6-175446	16 09 53.62	-17 54 47.4	145	M3	2.2	II	<4.5e-6	:/:/:	
S-35	J160959.4-180009	16 09 59.33	-18 00 09.1	145	M4	4.0	II	<5.1e-6	0/0/0/0	
S-36	J161115.3-175721	16 11 15.34	-17 57 21.4	145	M1	...	30.2	2.4	II	<6.3e-6	:/:/:	
S-37	HIP 79410	16 12 21.83	-19 34 44.6	140	B9V	<	D	<4.6e-6	:/:/:	
S-38	HIP 79439	16 12 44.11	-19 30 10.2	131	B9V	<	D	<3.9e-6	0/0/0	
S-39	J161402.1-230101	16 14 02.12	-23 01 02.2	145	G4	...	30.2	<	:/:/:	
S-40	J161411.0-230536	16 14 11.08	-23 05 36.2	145	K0	0.22	30.8	0.8	II	6.0e-6	0/0/0	
S-41	J161420.3-190648	16 14 20.30	-19 06 48.1	145	K5	...	29.3	5.2	II	1.7e-5	1/1/1/0	
S-42	HIP 79878	16 18 16.17	-28 02 30.1	129	A0V	<	D	<4.2e-6	0/0/0	
S-43	HIP 80088	16 20 50.23	-22 35 38.7	139	A9V	<	D	<3.7e-6	0/0/0	
S-44	HIP 80130	16 21 21.15	-22 06 32.3	144	A9V	<	...	<4.4e-6	:/:/:	
E-1	RECX18	08 36 10.7	-79 08 18.4	97	M5.3/M5.3	<0.04	30.6	...	III	...	:/:/:	
E-2	RECX1 (EG Cha)	08 36 56.24	-78 56 45.5	97	K7/M0	0.2	30.6	1.4	III	...	0/0/0	
E-3	RECX17	08 38 51.50	-79 16 13.7	97	M5.0/M5.0	<0.04	III	...	:/:/:	
E-4	RECX14 (ES Cha)	08 41 30.3	-78 53 06.5	97	M4.7	III	...	:/:/:	
E-5	RECX3 (EH Cha)	08 41 37.04	-79 03 30.4	97	M3.0	...	29.1	12	TO	3e-7	0/0/0	
E-6	RECX13 (HD75505)	08 41 44.72	-79 02 53.2	97	A5	2.2	TO	3.5e-10	0/0/0	
E-7	RECX4 (EI Cha)	08 42 23.73	-79 04 03.0	97	M1.3	...	30.1	...	III	...	:/:/:	
E-8	RECX5 (EK Cha)	08 42 27.11	-78 57 47.9	97	M3.8	...	29.0	2.3	TO	2e-9	0/0/0	
E-9	RECX6 (EL Cha)	08 42 38.80	-78 54 42.8	97	M3.0	...	29.5	3.6	TO	7e-6	0/0/0	

TABLE A1 (Continued)

ID	Name	RA	DEC	Dist.	Sp.T. ^a	Sep. ^b	log(L_p) ^c	W_{He} ^d	SED ^e	M_{disk}^f	OI/CH/ CO/H ₂ O ^g	Notes/refs. ^h
E-10	RECX7 (EM Cha)	08 43 07.24	-79 04 52.5	97	K6.9/M1	0.001	30.3	0.4	III	...	:/:/:	
E-11	RECX8 (RS Cha AB)	08 43 12.23	-79 04 12.3	97	A7/A8	eclipsing	29.8	<	III	...	0:/:/0	
E-12	RECX15 (ET Cha)	08 43 18.58	-79 05 18.2	97	M3.4	...	28.8	90	II	2.5e-8	1/0/0/0	Woi11
E-13	RECX16 (J0844.2-7833)	08 44 09.15	-78 33 45.7	97	M5.5	II	...	0:/:/0	
E-14	RECX9 (EN Cha)	08 44 16.38	-78 59 08.1	97	M4.4/M4.7	0.2	28.5	10	TO	1.4e-6	0:/:/0	
E-15	RECX10 (EO Cha)	08 44 31.88	-78 46 31.2	97	M0.3	...	30.0	1.0	III	...	0:/:/0	
E-16	RECX11 (EP Cha)	08 47 01.66	-78 59 34.5	97	K6.5	...	30.1	3.2	II	3.3e-5	1:/:/0	
E-17	RECX12 (EQ Cha)	08 47 56.77	-78 54 53.2	97	M3.2/M3.2	0.04	30.1	4.2	III	...	0:/:/0	
W-1	TWA21	10 13 14.76	-52 30 54.1	69	K3	...	30.2	3	III	<1.0e-6	:/:/:	
W-2	TWA07	10 42 30.11	-33 40 16.2	38	M1	...	29.6	5	TO	6.0e-7	0:/:/0	
W-3	TWA01 (TW Hya)	11 01 51.92	-34 42 17.0	58	M2.5	...	<30.4	220	II	6e-4	1/0/0/1	Thi10
W-4	TWA02AB	11 09 13.8	-30 01 39.8	52	M2	2	29.4	2	...	<1.0e-6	0:/:/0	
W-5	TWA03A (Hen3-600A)	11 10 27.88	-37 31 52.0	42	M3e	10	29.2	22	TO	1.1e-5	0:/:/0	
W-6	TWA12	11 21 05.50	-38 45 16.3	32	M2	...	29.1	51	...	<1.0e-6	:/:/:	
W-7	TWA13AB	11 21 17.24	-34 46 45.5	38	M2e	5.1	29.4	4	TO	...	0:/:/0	Confused region
W-8	TWA04AB (HD98000AB)	11 22 05.30	-24 46 39.3	46	M5	0.8	29.9	<	D	1e-6	1/0:/0	hierarchical
W-9	TWA05Aab	11 31 55.26	-34 36 27.2	50	M2	2	29.8	13.4	...	<1.0e-6	:/:/:	
W-10	TWA23	12 07 27.38	-32 47 00.3	37	M1	...	29.2	<	...	<1.0e-6	0:/:/0	
W-11	TWA25	12 15 30.72	-39 48 42.6	44	M0	...	29.8	2	...	<1.0e-6	:/:/:	
W-12	TWA16	12 34 56.30	-45 38 07.6	66	M1.5	0.7	29.6	4	...	<1.0e-6	:/:/:	
W-13	TWA10	12 35 04.25	-41 36 38.6	57	M2.5	...	29.6	11	...	<1.0e-6	0:/:/0	
B-1	HD 203	00 06 50.09	-23 06 27.1	39	F2IV	...	28.9	...	D	9e-9	:/:/:	
B-2	HD 14082B	02 17 25.02	+28 44 36.3	39	F5V	(10)	30.0	...	D	1.5e-8	:/:/:	SN03
B-3	AG Tri	02 27 29.25	+30 58 24.6	42	K8	(22)	D	>1.0e-10	:/:/:	SN03
B-4	HIP 12545	02 41 25.89	+05 59 18.4	41	M0	sb	...	0.6	:/:/:	
B-5	51 Eri (HD 29391)	04 37 36.13	-02 28 24.8	30	F0V	66	:/:/:	
B-6	GJ 3305	04 37 37.47	-02 29 28.4	30	M0.5	...	30.2	2.2	:/:/:	
B-7	AF Lep (HD 35850)	05 27 04.76	-11 54 03.5	27	F7V	sb	30.3	<	:/:/:	
B-8	AO Men	06 18 28.21	-72 02 41.5	39	K7	...	30.2	0.6	:/:/:	
B-9	HD 139084AB	15 38 57.23	-57 42 22.7	40	K0V	10.7	:/:/:	
B-10	HD 146624 (HR6070)	16 18 17.90	-28 36 50.5	43	A0V	:/:/:	
B-11	HD 164249	18 03 03.41	-51 38 56.4	47	F5V	16	30.6	<	D	>4e-10	0:/:/0	Ni109
B-12	HD 172555	18 45 26.90	-64 52 16.5	29	A7V	68.5	28.8	...	D	2e-9	1:/:/0	Ni109, Riv12.
B-13	CD-64 1208	18 45 37.03	-64 51 46.1	29	K7	0.2	29.9	:/:/:	
B-14	PZ Tel (HD 174429)	18 53 05.87	-50 10 49.9	50	K0Vp	0.3	30.6	<	D	(1e-8)	:/:/:	
B-15	η Tel AB (HD 181296)	19 22 51.21	-54 25 26.1	48	A0V	4.2	<28.9...D3e-8	...	D	3e-8	0:/:/0	
B-16	AT Mic AB (GJ 799A)	20 41 51.16	-32 26 06.8	10.2	M4.5e	3.3	29.4	10.9	0:/:/0	
B-17	HD 199143AB	20 55 47.67	-17 06 51.0	48	F8V	1.1	30.6	<	:/:/:	
B-18	HD 181327	19 22 58.94	-54 32 17.0	51	F5.5V	...	<29.4	...	D	1.5e-7	0/0/0/0	Ni109, Leb12
H-1	HD 105	00 05 52.55	-41 45 11.0	40	G0V	D	>2e-9	0:/:/0	Ni110, M06
H-2	HD 1466	00 18 26.12	-63 28 39.0	41	F9V	...	29.6	...	D	>3e-10	:/:/:	

TABLE A1 (Continued)

ID	Name	RA	DEC	Dist.	Sp.T. ^a	Sep. ^b	log(L_{\star}) ^c	$W_{\text{H}\alpha}$ ^d	SED ^e	M_{dust}^f	OI/CII/ CO/H ₂ O ^g	Notes/refs. ^h
H-3	HD 2884/5	00 31 33.07	-62 57 41.3	43	B9V/F2V	2.4/0.4	<28.8	...	D	...	:/:/:	Unassociated pair
H-4	HD 3003	00 32 43.91	-63 01 53.4	46	A0V	0.1	<28.7	...	D	>1e-10	0:/:0	
H-5	HD 3221	00 34 51.20	-61 54 58.1	46	K5V	...	30.0	0.7	:/:/:	
H-6	HIP 3556	00 45 28.15	-51 37 33.9	39	M1.5	0.8	:/:/:	
H-7	HD 12039 (DK Cet)	01 57 48.98	-21 54 05.3	42	G3/5V	0.2	29.6	...	D	>5e-10	:/:/:	
H-8	GSC8056-482	02 36 51.54	-52 03 04.4	25	M3Ve	...	29.7	5.3	:/:/:	
H-9	HD 16978 (ϵ Hyi)	02 39 35.36	-68 16 01.0	47	B9V	:/:/:	
H-10	HD 30051	04 43 17.20	-23 37 42.0	58	F2/F3IV/V	...	29.8	...	D	...	:/:/:	
H-11	HD 44627 (AB Pic)	06 19 12.91	-58 03 15.5	46	K2V	5.5	30.0	...	D	...	:/:/:	
H-12	HD 53842	06 46 13.54	-83 59 29.5	57	F5V	D	...	:/:/:	
H-13	HD 55279	07 00 30.49	-79 41 46.0	64	K3V	...	29.9	...	D	...	:/:/:	
H-14	HD 202917	21 20 49.96	-53 02 03.1	46	G5V	...	30.1	...	D	>5e-9	:/:/:	
H-15	HIP 107345	21 44 30.12	-60 58 38.9	42	M1	...	29.4	1.4	:/:/:	
H-16	HD 224392 (η Tuc)	23 57 35.08	-64 17 53.6	49	A1V	...	<29.3	:/:/:	
A-1	HD 9672 (49 Cet)	01 34 37.78	-15 40 34.9	59	A4V	D?	3e-7	0/1/0/0	Hu08, Zu12
A-2	HD 31648 (MWC480)	04 58 46.27	+29 50 37.0	137	A5V	...	29.4	...	gr.II	3.6e-4	1/0/1/1	Jet
A-3	HD 32297	05 02 27.44	+07 27 39.7	112	A0	D	3e-6	0/0/0/0	Ma08
A-4	HD 35187	05 24 01.17	+24 57 37.6	114	A2V/A7V	1.4	gr.II	5e-5	1/0/0/0	
A-5	HD 36112 (MWC758)	05 30 27.53	+25 19 57.1	279	A5IV	gr.I	3e-5	1/0/1/0	Cha08
A-6	HD 36910 (CQ1au)	05 35 58.47	+24 44 54.1	113	F2Ve	gr.II	1e-5	1/0/1/0	Cha08
A-7	HR 1998 (ζ Lep)	05 46 57.34	-14 49 19.0	22	A2V	D	>3e-12	0/0/0/0	Mo07
A-8	HD 97048 (CU Cha)	11 08 03.34	-77 39 17.5	158	A0	...	29.5	...	gr.I	9.2e-4	1/1/1/0	Sk04
A-9	HD 100453	11 33 05.58	-54 19 28.5	121	A9V	1.1	28.8	...	gr.I	2.1e-4	1/0/0/0	Co09
A-10	HD 100546	11 33 25.44	-70 11 41.2	97	B9V	...	28.9	...	gr.I	2.9e-4	1/1/1/0	Fei03, Gra05
A-11	HD 104237 (DX Cha)	12 00 05.08	-78 11 34.6	115	A8	sb	30.2	...	gr.II	7.8e-5	1/0/0/0	Jet, Fei03
A-12	HR 4796A (TWA11)	12 36 01.0	-39 52 10.2	73	A0	7.8	29.4	...	D	1e-5	0/0/0/0	Aug99
A-13	HD 135344B (SAO 206462)	15 15 48.4	-37 09 16.0	142	F4V	...	29.7	...	gr.I	1.6e-4	1/0/0/0	Pon08
A-14	HD 139614	15 40 46.38	-42 29 53.5	140	A7V	gr.I	2.7e-4	1/0/0/0	Ack04
A-15	HD 141569	15 49 57.75	-03 55 16.4	116	B9.5V	...	<28.1	...	TO?	1e-6	1/1/0/0	Site06
A-16	HD 142666 (V1026Sco)	15 56 40.02	-22 01 40.0	145	A8V	gr.II	1.6e-4	1/0/0/0	
A-17	HD 142527	15 56 41.89	-42 19 23.3	233	F6III	gr.I	1.5e-3	1/0/0/0	Ack04
A-18	HD 144668 (HR 5999)	16 08 34.29	-39 06 18.3	163	A7IVe	1.2	28.3	...	gr.II	9e-5	1/0/1/0	Site10
A-19	HD 150193 (MWC863)	16 40 17.92	-23 53 45.2	216	A2IVe	1.1	29.6	...	gr.II	2e-5	1/0/0/0	Site06
A-20	KK OphAB	17 10 08.06	-27 15 18.2	260	A6/G5V	1.6	gr.II	2e-5	1/1/1/0	
A-21	HD 158352 (HR 6507)	17 28 49.65	+00 19 50.2	60	A7Vp	D	2e-7	0/0/0/0	Rh07
A-22	HD 158643 (51 Oph)	17 31 24.95	-23 57 45.5	124	B9.5V	...	<29.0	...	gr.II	1e-6	1/0/0/0	vdA01
A-23	HD 163296 (MWC275)	17 56 21.29	-21 57 21.9	119	A1V	...	29.6	...	gr.II	6.5e-4	1/0/1/1	Jet, GS09, Till12
A-24	HD 169142 (MWC925)	18 24 29.78	-29 46 49.4	145	A7V	9.3	29.1	...	gr.I	2.4e-4	1/0/1/0	Gra07, Meul10
C-1	DK Cha	12 53 17.23	-77 07 10.7	178	F0	...	<29.0	88	II	4.0e-3	1/1/0	Ext.OI, jet, vK10
C-2	IRAS12500-7658	12 53 42.86	-77 15 11.5	178	M6.5	...	<29.3	20	I	...	1/1/0	
C-3	Sz46N	12 56 33.66	-76 45 45.3	178	M1	...	29.3	16	II	5.0e-5	0/1/0	
C-4	IRAS12535-7623	12 57 11.77	-76 40 11.3	178	M0	...	29.3	15	II	1.6e-4	0/1/0	
C-5	ISO-ChaII 13	12 58 06.78	-77 09 09.4	178	M7	101	II	1.6e-6	0/1/0	
C-6	Sz50	13 00 55.36	-77 10 22.1	178	M3	...	29.5	29	II	1.0e-3	1/1/0	

TABLE A1 (Continued)

ID	Name	RA	DEC	Dist.	Sp. T. ^a	Sep. ^b	$\log(L_{\star})^c$	$W_{\text{H}\alpha}^d$	SED ^e	M_{dust}^f	OI/CH/ CO/H ₂ O ^g	Notes/refs. ^h
C-7	Sz51	13 01 58.94	-77 51 21.7	178	K8.5	...	<29.5	102	II	5.0e-5	1/:/0	
C-8	C50	13 02 22.85	-77 34 49.3	178	M5	36	II	1.0e-6	0/:/0	
C-9	Sz52	13 04 24.92	-77 52 30.1	178	M2.5	...	<30.9	48	II	8.0e-4	1/:/0	
C-10	Hn25	13 05 08.53	-77 33 42.4	178	M2.5	...	<29.2	24	II	1.0e-5	0/:/0	
C-11	Sz53	13 05 12.69	-77 30 52.3	178	M1	...	<29.0	46	II	1.0e-5	0/:/0	
C-12	Sz54	13 05 20.68	-77 39 01.4	178	K5	...	28.6	23	II	5.0e-4	1/:/0	
C-13	J130521.6-773810	13 05 21.66	-77 38 10.0	178	29	I-II	1.0e-6	1/:/0	Embedded?
C-14	J130529.0-774140	13 05 29.04	-77 41 40.1	178	II	...	0/:/0	
C-15	C62	13 07 18.05	-77 40 52.9	178	M4.5	34	II	1.0e-5	0/:/0	
C-16	Hn26	13 07 48.51	-77 41 21.4	178	M2	...	<29.1	10	II	1.0e-5	0/:/0	
C-17	Sz61	13 08 06.28	-77 55 05.2	178	K5	...	<31.0	84	II	1.6e-3	1/:/0	
C-18	C66	13 08 27.17	-77 43 23.2	178	M4.5	30	II	1.0e-6	0/:/0	
C-19	Sz62	13 09 50.38	-77 57 23.9	178	M2.5	1.1	<32.4	150	II	1.0e-6	0/:/0	

NOTE.—Table A1 is ordered by association or group, and RA Coordinates are the pointing positions of the observations, and may be centered between multiple systems. Key to the naming convention is: T = Taurus, S = Upper Sco, E = η Cha, W = TW Hya, B = β Pic Moving group, H = Tuc Hor, A = Herbig AeBe stars and A stars with debris disks (noted in column 10 as D) and C = ChaII.

References.—(Ack04) Acke et al. 2004; (Aug99) Augereau et al. 1999; (Cha08) Chapillon et al. 2008; (Co09) Collins et al. 2009; (Fei03) Feigelson et al. 2003; (Gra05) Grady et al. 2005; (Gra07) Grady et al. 2007; (GS09) Gunther & Schmitt 2009; (Hu08) Hughes et al. 2008; (Leb12) Lebreton et al. 2012; (Ma08) Maness et al. 2008; (Meu10) Meeus et al. 2010; (Mo07) Moerchen et al. 2007; (M04) Mamajek et al. 2004; (M06) Moór et al. 2006; (Nil09) Nilsson et al. 2009; (Nil10) Nilsson et al. 2010; (Po12) Podio et al. 2012; (Pon08) Pontoppidan et al. 2008; (Rho07) Rhee et al. 2007; (Riv12) Riviere-Marichalar et al. 2012b; (Ski04) Skinner et al. 2004; (Smi06) Smith et al. 2006; (SN03) Song et al. 2003; (Ste06) Stelzer et al. 2006; (Thi12) Tilling et al. 2012; (Thi10) Thi et al. 2010; (vdA01) van den Ancker et al. 2001; (vK10) van Kempen et al. 2010; (Woi11) Woitke et al. 2011; (Zu12) Zuckerman & Song 2012. Additional references are given in the text.

^aSpectral type. For multiple systems, we give either only the primary or the brightest components when these are separable in PACS.

^bFor multiple systems, separation, in arcsec, between the two main components. 'sb' indicates a spectroscopic binary.

^cX-ray luminosity, between 0.3 and 10 keV, in erg s^{-1} .

^dH α EW is given as positive for an emission component, '<' for photospheric absorption, and blank for no measurement. An average from published values for the most luminous component is indicated, or both components when they are separable with PACS. Note that the H α EW is highly variable in many objects.

^eSED Class from the literature, if available: I-II, II (defined as $-0.3 > \alpha_{\text{IR}} > -1.6$), III ($\alpha_{\text{IR}} < -1.6$), which includes stars without a measured IR excess), TO (Transition Object, defined as a Class III object with an additional excess at wavelengths longer than 10 μm), or D (classified as a debris disk). Note that for the Herbig AeBe stars, the SED classification is instead based on the Meeus SED groups I and II—see § 5.0.9 for details. Blank means no excess is known in either the IR or longer wavelengths.

^fDisk d_{dust} mass, in Solar units, derived in most cases from published mm/sub-mm observations (see § 5.0 for references). Upper limits are $3\text{-}\sigma$, and a dashed line indicates no published values were available. Lower limits are normally based on fits to FIR photometry, where no sub-mm datapoint is available. Note that disk mass for protoplanetary disks is normally assumed to be $100 M_{\text{dust}}$.

^gSummary of line detections from PACS of [OI]63 μm , [CII]157 μm , CO J-18-17 and H₂O (any transition detected, most commonly the line at 63.3 μm —see text). '1' indicates detection, '0' means not detected, '+' means not observed.

^h'Jet' indicates published evidence of an optical jet, 'Ext.OI' indicates the [OI]63 μm emission appears extended and 'high M' ' indicates published high mass loss rate (see § 5.2.1 and 5.2.2 for details). 'Mult.' indicates a multiple hierarchical system.

ⁱMembership is now in doubt—see Luhman et al. (2009).

REFERENCES

- Abel, N. P., Sarma, A. P., Troland, T. H., & Ferland, G. J. 2007, *ApJ*, 662, 1024
- Acke, B., van den Ancker, M. E., & Dullemond, C. P. 2005, *A&A*, 436, 209
- Acke, B., van den Ancker, M. E., Dullemond, C. P., van Boekel, R., & Waters, L. B. F. M. 2004, *A&A*, 422, 621
- Alcalá, J. M., Covino, E., Sterzik, M. F., et al. 2000, *A&A*, 355, 629
- Alcalá, J. M., Spezzi, L., Chapman, N., et al. 2008, *ApJ*, 676, 427
- André, P., Men'shchikov, A., Bontemps, S., et al. 2010, *A&A*, 518, L102
- Andrews, S. M., & Williams, J. P. 2005, *ApJ*, 631, 1134
- Arce, H. G., & Sargent, A. I. 2006, *ApJ*, 646, 1070
- Ardila, D. R., Golimowski, D. A., & Krist, J. E., et al. 2007, *ApJ*, 665, 512
- Aresu, G., Kamp, I., Meijerink, R., et al. 2011, *A&A*, 526, A163
- Augereau, J. C., Lagrange, A. M., Mouillet, D., Papaloizou, J. C. B., & Grorod, P. A. 1999, *A&A*, 348, 557
- Barrado Y Navascués, D. 2006, *A&A*, 459, 511
- Barrado y Navascués, D., Stauffer, J. R., Song, I., & Caillaud, J.-P. 1999, *ApJ*, 520, L123
- Benedettini, M., Viti, S., Giannini, T., Nisini, B., Goldsmith, P. F., & Saraceno, P. 2002, *A&A*, 395, 657
- Boissier, J., Alonso-Albi, T., Fuente, A., et al. 2011, *A&A*, 531, A50
- Bontemps, S., André, P., Terebey, S., & Cabrit, S. 1996, *A&A*, 311, 858
- Borucki, W. J., Koch, D. G., Basri, G., et al. 2011, *ApJ*, 736, 19
- Bouwman, J., Lawson, W. A., Dominik, C., Feigelson, E. D., Henning, T., Tielens, A. G. G. M., & Waters, L. B. F. M. 2006, *ApJ*, 653, L57
- Brandeker, A. 2011, *AAS/Division for Extreme Solar Systems Abstracts*, 2, 3802
- Bryden, G., et al. 2009, *ApJ*, 705, 1226
- Carpenter, J. M., et al. 2009, *ApJS*, 181, 197
- Chapillon, E., Guilloteau, S., Dutrey, A., & Piétu, V. 2008, *A&A*, 488, 565
- Chen, C. H., Li, A., Bohac, C., et al. 2007, *ApJ*, 666, 466
- Clampin, M., Krist, J. E., Ardila, D. R., et al. 2003, *AJ*, 126, 385
- Cohen, M., Hollenbach, D. J., Haas, M. R., & Erickson, E. F. 1988, *ApJ*, 329, 836
- Collins, K. A., Grady, C. A., Hamaguchi, K., et al. 2009, *ApJ*, 697, 557
- Creech-Eakman, M. J., Chiang, E. I., Joun, R. M. K., Blake, G. A., & van Dishoeck, E. F. 2002, *A&A*, 385, 546
- Currie, T., & Sicilia-Aguilar, A. 2011, *ApJ*, 732, 24
- D'Alessio, P., Calvet, N., Hartmann, L., Franco-Hernández, R., & Servín, H. 2006, *ApJ*, 638, 314
- de la Reza, R., & Pinzón, G. 2004, *AJ*, 128, 1812
- de Zeeuw, P. T., Hoogerwerf, R., de Bruijne, J. H. J., Brown, A. G. A., & Blaauw, A. 1999, *AJ*, 117, 354
- Dent, W. R. F., Greaves, J. S., Mannings, V., Coulson, I. M., & Walther, D. M. 1995, *MNRAS*, 277, L25
- Dent, W. R. F., Greaves, J. S., & Coulson, I. M. 2005, *MNRAS*, 359, 663
- D'Orazi, V., Biazzo, K., & Randich, S. 2011, *A&A*, 526, A103
- Donaldson, J. K., Roberge, A., Chen, C. H., et al. 2012, *ApJ*, 753, 147
- Dullemond, C. P., & Dominik, C. 2005, *A&A*, 434, 971
- Ercolano, B., Bastian, N., Spezzi, L., & Owen, J. 2011, *MNRAS*, 416, 439
- Evans, N. J., et al. 2009, *ApJS*, 181, 321
- Feigelson, E. D., Lawson, W. A., & Garmire, G. P. 2003, *ApJ*, 599, 1207
- Fischer, D., & Valenti, J. 2005, *ApJ*, 622, 1102
- Franklin, J., Snell, R. L., Kaufman, M. J., Melnick, G. J., Neufeld, D. A., Hollenbach, D. J., & Bergin, E. A. 2008, *ApJ*, 674, 1015
- Fuente, A., Martn-Pintado, J., Bachiller, R., Rodriguez-Franco, A., & Palla, F. 2002, *A&A*, 387, 977
- Furlan, E., Hartmann, L., Calvet, N., et al. 2006, *ApJS*, 165, 568
- Gautier, T. N., III, Rebull, L. M., Stapelfeldt, K. R., & Mainzer, A. 2008, *ApJ*, 683, 813
- Giannini, et al. 1999, *A&A*, 346, 617
- Goicoechea, J. R., Cernicharo, J., Karska, A., et al. 2012, *A&A*, 548, A77
- Gorti, U., & Hollenbach, D. 2004, *ApJ*, 613, 424
- . 2008, *ApJ*, 683, 287
- . 2009, *ApJ*, 690, 1539
- Gorti, U., Hollenbach, D., Najita, J., & Pascucci, I. 2011, *ApJ*, 735, 90
- Grady, C. A., Schneider, G., Hamaguchi, K., et al. 2007, *ApJ*, 665, 1391
- Grady, C. A., Woodgate, B., Heap, S. R., Bowers, C., Nuth, J. A., Herczeg, G. J., & Hill, H. G. M. 2005, *ApJ*, 620, 470
- Greaves, J. S., Fischer, D. A., & Wyatt, M. C. 2006, *MNRAS*, 366, 283
- Güdel, M., Briggs, K. R., Arzner, K., et al. 2007, *A&A*, 468, 353
- Güdel, M., Lahuis, F., Briggs, K. R., et al. 2010, *A&A*, 519, A113
- Günther, H. M., & Schmitt, J. H. M. M. 2009, *A&A*, 494, 1041
- Haisch, K. E., Jr., Lada, E. A., & Lada, C. J. 2001, *ApJ*, 553, L153
- Harris, R. J., Andrews, S. M., Wilner, D. J., & Kraus, A. L. 2012, *ApJ*, 751, 115
- Hartigan, P., Edwards, S., & Ghandour, L. 1995, *ApJ*, 452, 736
- Hartmann, L. 2001, *AJ*, 121, 1030
- Hartmann, L., Calvet, N., Gullbring, E., & D'Alessio, P. 1998, *ApJ*, 495, 385
- Hillenbrand, L. A., Carpenter, J. M., Kim, J. S., et al. 2008, *ApJ*, 677, 630
- Hioki, T., Itoh, Y., Oasa, Y., et al. 2007, *AJ*, 134, 880
- Hollenbach, D. 1985, *Icarus*, 61, 36
- Hollenbach, D. J., Takahashi, T., & Tielens, A. G. G. M. 1991, *ApJ*, 377, 192
- Hollenbach, D. J., & Tielens, A. G. G. M. 1997, *ARA&A*, 35, 179
- Hughes, A. M., Wilner, D. J., Kamp, I., & Hogerheijde, M. R. 2008, *ApJ*, 681, 626
- Hughes, A. M., Wilner, D. J., Andrews, S. M., et al. 2011, *ApJ*, 740, 38
- Johnson, J. A., Butler, R. P., Marcy, G. W., Fischer, D. A., Vogt, S. S., Wright, J. T., & Peek, K. M. G. 2007, *ApJ*, 670, 833
- Jonkheid, B., Faas, F. G. A., van Zadelhoff, G.-J., & van Dishoeck, E. F. 2004, *A&A*, 428, 511
- Kalas, P., Graham, J. R., Chiang, E., et al. 2008, *Science*, 322, 1345
- Kamp, I., van Zadelhoff, G.-J., van Dishoeck, E. F., & Stark, R. 2003, *A&A*, 397, 1129
- Kamp, I., & Sammar, F. 2004, *A&A*, 427, 561
- Kamp, I., Tilling, I., Woitke, P., Thi, W.-F., & Hogerheijde, M. 2010, *A&A*, 510, A18
- Kamp, I., Woitke, P., Pinte, C., et al. 2011, *A&A*, 532, A85
- Kastner, J. H., Zuckerman, B., Weintraub, D. A., & Forveille, T. 1997, *Science*, 277, 67

- Kenyon, S., & Hartmann, L. 1995, *ApJS*, 101, 117
- Kenyon, S. J., Brown, D. I., Tout, C. A., & Berlind, P. 1998, *AJ*, 115, 2491
- Kenyon, S. J., Gómez, M., & Whitney, B. A. 2008, *Handbook of Star Forming Regions, Volume I* (San Francisco: ASP), 405
- Krivov, A. V., Müller, S., Löhne, T., & Mutschke, H. 2008, *ApJ*, 687, 608
- Lagrange, A.-M., Beust, H., Mouillet, D., et al. 1998, *A&A*, 330, 1091
- Lahuis, F., van Dishoeck, E. F., Blake, G. A., Evans, N. J., II, Kessler-Silacci, J. E., & Pontoppidan, K. M. 2007, *ApJ*, 665, 492
- Lebreton, J., Augereau, J.-C., Thi, W.-F., et al. 2012, *A&A*, 539, A17
- Liseau, R., Justtanont, K., & Tielens, A. G. G. M. 2006, *A&A*, 446, 561
- López-Santiago, J., Albacete Colombo, J. F., & López-García, M. A. 2010, *A&A*, 524, A97
- Lorenzetti, D., Giannini, T., Nisini, B., et al. 2000, *A&A*, 357, 1035
- Low, F. J., Smith, P. S., Werner, M., Chen, C., Krause, V., Jura, M., & Hines, D. C. 2005, *ApJ*, 631, 1170
- Luhman, K. L., Allen, P. R., Espaillat, C., Hartmann, L., & Calvet, N. 2010, *ApJS*, 186, 111
- Luhman, K. L., Mamajek, E. E., Allen, P. R., & Cruz, K. L. 2009, *ApJ*, 703, 399
- Maldonado, J., Eiroa, C., Villaver, E., Montesinos, B., & Mora, A. 2012, *A&A*, 541, A40
- Mamajek, E. E. 2005, *ApJ*, 634, 1385
- Mamajek, E. E., Meyer, M. R., Hinz, P. M., Hoffmann, W. F., Cohen, M., & Hora, J. L. 2004, *ApJ*, 612, 496
- Mamajek, E. E., Lawson, W. A., & Feigelson, E. D. 1999, *ApJ*, 516, L77
- Maness, H. L., Fitzgerald, M. P., Paladini, R., et al. 2008, *ApJ*, 686, L25
- Mathews, G. S., Dent, W. R. F., Williams, J. P., et al. 2010, *A&A*, 518, L127
- Mathews, G. S., Williams, J. P., Ménard, F., et al. 2012, *ApJ*, 745, 23
- Matthews, B. C., Kalas, P. G., & Wyatt, M. C. 2007, *ApJ*, 663, 1103
- Meijerink, R., Glassgold, A. E., & Najita, J. R. 2008, *ApJ*, 676, 518
- Meeus, G., Montesinos, B., Mendigutía, I., et al. 2012, *A&A*, 544, A78
- Meeus, G., Pinte, C., Woitke, P., et al. 2010, *A&A*, 518, L124
- Meeus, G., Waters, L. B. F. M., Bouwman, J., et al. 2001, *A&A*, 365, 476
- Melnikov, S. Y., Eisloffel, J., Bacciotti, F., Woitas, J., & Ray, T. P. 2009, *A&A*, 506, 763
- Moerchen, M. M., Telesco, C. M., Packham, C., & Kehoe, T. J. 2007, *ApJ*, 655, L109
- Molinari, S., Noriega-Crespo, A., Ceccarelli, C., Nisini, B., Giannini, T., Lorenzetti, D., Caux, E., Liseau, R., et al. 2000, *A&A*, 538, 698
- Montesinos, B., Eiroa, C., Mora, A., & Merín, B. 2009, *A&A*, 495, 901
- Moór, A., Abraham, P., Derekas, A., et al. 2006, *ApJ*, 644, 525
- Najita, J. R., Carr, J. S., Strom, S. E., Watson, D. M., Pascucci, I., Hollenbach, D., Gorti, U., & Keller, L. 2010, *ApJ*, 712, 274
- Nilsson, R., Liseau, R., Brandeker, A., et al. 2009, *A&A*, 508, 1057
- Nilsson, R., Liseau, R., Brandeker, A., Olofsson, G., Pilbratt, G. L., Risacher, C., Rodmann, J., Augereau, J.-C., et al. 2010, *A&A*, 518, 40
- Nisini, B., Benedettini, M., Giannini, T., Codella, C., Lorenzetti, D., di Giorgio, A. M., & Richer, J. S. 2000, *A&A*, 360, 297
- Nisini, B., Giannini, T., & Lorenzetti, D. 2002, *ApJ*, 576, 246
- Öberg, K. I., et al. 2010, *ApJ*, 720, 480
- Olofsson, G., Liseau, R., & Brandeker, A. 2001, *ApJ*, 563, L77
- Ott, S. 2010, *ASP Conf. Ser.*, 434, 139
- Palla, F., & Stahler, S. W. 2002, *ApJ*, 581, 1194
- Pascucci, I., & Sterzik, M. 2009, *ApJ*, 702, 724
- Pecaut, M. J., Mamajek, E. E., & Bubar, E. J. 2012, *ApJ*, 746, 154
- Pilbratt, G. L., Riedinger, J. R., Passvogel, T., et al. 2010, *A&A*, 518, L1
- Pinte, C., Harries, T. J., Min, M., et al. 2009, *A&A*, 498, 967
- Pinte, C., Ménard, F., Duchêne, G., & Bastien, P. 2006, *A&A*, 459, 797
- Pinte, C., Woitke, P., Ménard, F., et al. 2010, *A&A*, 518, L126
- Podio, L., Kamp, I., Flower, D., et al. 2012, *A&A*, 545, A44
- Poglitsch, A., et al. 2010, *A&A*, 518, L2
- Pontoppidan, K. M., Blake, G. A., van Dishoeck, E. F., Smette, A., Ireland, M. J., & Brown, J. 2008, *ApJ*, 684, 1323
- Pontoppidan, K. M., Salyk, C., Blake, G. A., et al. 2010, *ApJ*, 720, 887
- Rebull, L. M., et al. 2008, *ApJ*, 681, 1484
- Rebull, L. M., Padgett, D. L., McCabe, C.-E., et al. 2010, *ApJS*, 186, 259
- Rhee, J. H., Song, I., Zuckerman, B., & McElwain, M. 2007, *ApJ*, 660, 1556
- Rice, W. K. M., Armitage, P. J., Wood, K., & Lodato, G. 2006, *MNRAS*, 373, 1619
- Riviere-Marichalar, P., Barrado, D., Augereau, J.-C., et al. 2012a, *A&A*, 546, L8
- Riviere-Marichalar, P., Ménard, F., Thi, W. F., et al. 2012b, *A&A*, 538, L3
- Roberge, A., Feldman, P. D., Weinberger, A. J., Deleuil, M., & Bouret, J.-C. 2006, *Nature*, 441, 724
- Sandell, G., Weintraub, D. A., & Hamidouche, M. 2011, *ApJ*, 727, 26
- Scholz, A., Coffey, J., Brandeker, A., & Jayawardhana, R. 2007, *ApJ*, 662, 1254
- Shibai, H., et al. 1991, *ApJ*, 374, 522
- Sicilia-Aguilar, A., Bouwman, J., Juhász, A., et al. 2009, *ApJ*, 701, 1188
- Skinner, S. L., Güdel, M., Audard, M., & Smith, K. 2004, *ApJ*, 614, 221
- Smith, P. S., Hines, D. C., Low, F. J., Gehr, R. D., Polomski, E. F., & Woodward, C. E. 2006, *ApJ*, 644, L125
- Song, I., Zuckerman, B., & Bessell, M. S. 2003, *ApJ*, 599, 342
- Spezzi, L., Alcalá, J. M., Covino, E., et al. 2008, *ApJ*, 680, 1295
- Spinoglio, L., et al. 2000, *A&A*, 353, 1055
- Stacey, G. J., Geis, N., Genzel, R., et al. 1991, *ApJ*, 373, 423
- Stelzer, B., Micela, G., Hamaguchi, K., & Schmitt, J. H. M. M. 2006, *A&A*, 457, 223
- Thalmann, C., Grady, C. A., Goto, M., et al. 2010, *ApJ*, 718, L87
- Thébaud, P., & Augereau, J.-C. 2005, *A&A*, 437, 141
- Thi, W.-F., van Dalen, B., Bik, A., Waters, L. F. B. M. 2005, *A&A*, 430, L61
- Thi, W.-F., Mathews, G., Ménard, F., et al. 2010, *A&A*, 518, L125
- Thi, W.-F., Ménard, F., Meeus, G., et al. 2011, *A&A*, 530, L2
- Tilling, I., Woitke, P., Meeus, G., et al. 2012, *A&A*, 538, A20
- Torres, C. A. O., da Silva, L., Quast, G. R., de la Reza, R., & Jilinski, E. 2000, *AJ*, 120, 1410
- Torres, C. A. O., Quast, G. R., Melo, C. H. F., & Sterzik, M. F. 2008, *Handbook of Star Forming Regions, Volume II*, 757
- Torres, R. M., Loinard, L., Mioduszewski, A. J., & Rodríguez, L. F. 2009, *ApJ*, 698, 242
- Trilling, D. E., et al. 2007, *ApJ*, 658, 1289

- Trilling, D. E., Bryden, G., Beichman, C. A., et al. 2008, *ApJ*, 674, 1086
- van den Ancker, M. E., Meeus, G., Cami, J., Waters, L. B. F. M., & Waelkens, C. 2001, *A&A*, 369, L17
- van Dishoeck, E. F. 2004, *ARA&A*, 42, 119
- van Kempen, T. A., Kristensen, L. E., Herczeg, G. J., et al. 2010, *A&A*, 518, L121
- Webb, R. A., Zuckerman, B., Platais, I., Patience, J., White, R. J., Schwartz, M. J., & McCarthy, C. 1999, *ApJ*, 512, L63
- Whittet, D. C. B., Prusti, T., Franco, G. A. P., et al. 1997, *A&A*, 327, 1194
- Williams, J. P., & Cieza, L. A. 2011, *ARA&A*, 49, 67
- Woitke, P., Kamp, I., & Thi, W-F. 2009a, *A&A*, 501, 383
- Woitke, P., Thi, W-F., Kamp, I., & Hogerheijde, M. R. 2009b, *A&A*, 501, L5
- Woitke, P., Pinte, C., Tilling, I., et al. 2010, *MNRAS*, 405, L26
- Woitke, P., Riaz, B., Duchêne, G., et al. 2011, *A&A*, 534, A44
- Wyatt, M. C. 2008, *ARA&A*, 46, 339
- Wyatt, M. C., Dent, W. R. F. 2002, *MNRAS*, 334, 589
- Young, K. E., Harvey, P. M., Brooke, T. Y., et al. 2005, *ApJ*, 628, 283
- Zagorovsky, K., Brandeker, A., & Wu, Y. 2010, *ApJ*, 720, 923
- Zuckerman, B., Forveille, T., & Kastner, J. H. 1995, *Nature*, 373, 494
- Zuckerman, B., & Song, I. 2012, *ApJ*, 758, 77
- Zuckerman, B., Rhee, J. H., Song, I., & Bessell, M. S. 2011, *ApJ*, 732, 61
- Zuckerman, B., Song, I., Bessell, M. S., & Webb, R. A. 2001, *ApJ*, 562, L87
- Zuckerman, B., & Webb, R. A. 2000, *ApJ*, 535, 959